Colloids and Surfaces A: Physicochemical and Engineering Aspects 677 (2023) 132446

Contents lists available at ScienceDirect

Colloids and Surfaces A: Physicochemical and Engineering Aspects

journal homepage: www.elsevier.com/locate/colsurfa

The green synthesis of carbon quantum dots (CQDs) and characterization of polycaprolactone (PCL/CQDs) films

F. Mindivan [a,*], M. Göktaş [b]

[a] Bilecik Seyh Edebali University, Faculty of Engineering, Department of Bioengineering, Bilecik 11230, Turkey
[b] Bilecik Seyh Edebali University, Vocational College, Department of Metallurgy, Bilecik 11230, Turkey

GRAPHICAL ABSTRACT

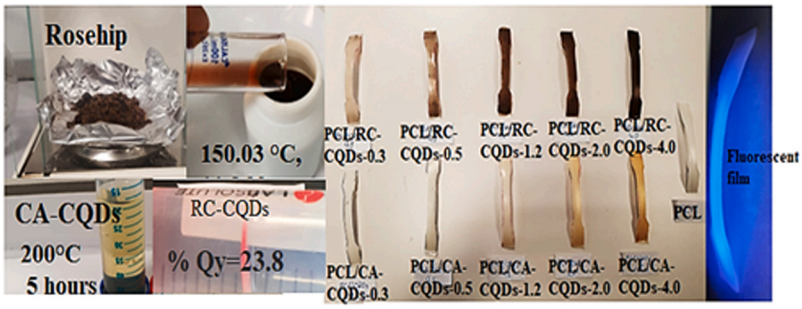

ARTICLE INFO

Keywords:
Rosa canina L.
Carbon quantum dots
Quantum yield
Polycaprolactone nanocomposite films
Mechanical properties
Biodegradability

ABSTRACT

The synthesis of photoluminescent carbon quantum dots (CQD) from natural products is one of the most remarkable types of carbon-based nanomaterials due to their small size, high water solubility, nontoxicity, high stability, and excellent biocompatibility. New RC-CQDs have been prepared from natural material (rosehip fruit) via a hydrothermal method. CA-CQDs samples were synthesized from a synthetic carbon source (citric acid) by the same method for comparison with RC-CQDs. The maximum quantum yields of the as-prepared RC-CQDs and CA-CQDs samples were 23.8% and 9.6%, respectively. High-resolution transmission electron microscopy (RTEM) of RC-CQDs revealed a sphere shape with an approximate size of 5 nm, CA-CQDs were greater than 5 nm. Biodegradable polycaprolactone (PCL), which is used in bioengineering applications thanks to its mechanical and biodegradable properties, was used as a polymer matrix in this study. The PCL/RC-CQDs and PCL/CA-CQDs nanocomposite films were produced via liquid phase ultrasonic mixing at different amounts of RC-CQDs and CA-CQDs in PCL matrix (0.3-; 0.5-; 1.2-; 2.0% and 4.0% by weight), while unfilled PCL was also produced for comparison. The structural, mechanical, and biodegradable behaviors of PCL/RC-CQDs nanocomposite films have been investigated to improve the mechanical properties of PCL and increase its potential usability in load-bearing applications. PCL/RC-CQDs-2.0 film gave the maximum tensile strength value (17.65 MPa) with an increment of 27.7% and the highest value of the yield strength 9.02 MPa (an increase of 40.9%) and the highest value of microhardness 4.80 $HV_{0,025}$ (an increase of 14.8%) were obtained using PCL/RC-CQDs-4.0 film compared with the PCL. The tensile strength and % elongation at break values of the PCL/CA-CQDs-0.3 film decreased by 14.8% and 133.1% compared with the PCL, respectively. The microhardness of the PCL/CA-CQDs-

* Corresponding author.
E-mail address: ferda.mindivan@bilecik.edu.tr (F. Mindivan).

https://doi.org/10.1016/j.colsurfa.2023.132446
Received 16 June 2023; Received in revised form 2 September 2023; Accepted 19 September 2023
Available online 21 September 2023

0.3 film was 5.48 $HV_{0,025}$, increasing by 31.1% in comparison with 4.18 $HV_{0,025}$, for the PCL. Biodegradability test results showed that films containing RC-CQDs exhibited lower weight loss than the PCL and films containing CA-CQDs. This result was attributed to the amorphous structure, low surface roughness and high contact angle of the RC-CQDs containing films. And also, CA-CQDs made PCL films more hydrophilic according to low contact angle results.

1. Introduction

The carbon quantum dots (CQDs) is an amorphous or nanocrystalline, zero-dimensional, hemispherical allotrope of carbon with extremely small particle sizes (about 2–5 nm) containing sp^2 and sp^3 hybrid carbon atoms [1,2]. Since their discovery, CQDs have been the focus of many studies due to their unique properties, such as exceptional solubility, easy functionalization, chemical stability, high photoluminescence, less toxicity, and resistance to photobleaching compared to one-dimensional carbon nanostructures. These outstanding properties have made them remarkable materials in a variety of applications such as optoelectronics, bioimaging, fluorescent sensors, biosensing, white light emitting diodes (WLED), and solar cells [2]. Currently, studies on CQDs all over the world are divided into two groups. The first is the newly discovered beginning materials for CQDs production, and the second is the optimization of CQDs synthesis to provide size, shape control and high quantum yield [3]. A high quantum yield is frequently the major goal of scientists creating luminous materials. Excitation energy is converted into photons by luminescent materials, however this conversion is typically not 100% efficient because of various losses. Each photon that is absorbed causes an emission, which is referred to as a quantum yield [4]. The top-down approach used to generate the CQDs: It includes laser ablation, arc discharge, electrochemical and chemical oxidation, ultrasonic synthesis, and a bottom-up approach (bottom-up): synthesis techniques known as microwave synthesis, thermal and plasma degradation, and the hydrothermal method [5]. The laser ablation technique is very fast, but this method is not economically preferred and is known as a complex process. Chemical methods are commonly considered to avoid the use of expensive beginning materials and energy systems. In addition, gas and carbon residues or the oxidation of activated carbon with strong acids such as nitric acid are considered relatively inexpensive ways to synthesize CQDs. However, the use of strong acids in large quantities is the disadvantage of this method. The carbonization of molecular precursors such as glucose, sucrose, glycerol, citric acid, and ascorbic acid to produce fluorescent CQDs has received great attention in this field. This method is not preferred because of the multi-step processes and the use of acids as well as surface passivating agents [3]. Among these methods, the hydrothermal method is economically advantageous because it is carried out in a single environment and has simple and low-temperature applications. It is also accepted as a green synthetic approach with its use in aqueous solution and better quantum yield [6]. Today, the green synthesis approach has paved the way for the sustainable synthesis of CQDs by focusing on the design of products and processes that minimize the use of strong chemicals in production. The use of renewable starting materials and environmentally friendly, non-toxic chemicals are one of the main targets of this approach [3,7]. In general, natural resources such as plant leaves, fruit juices, and fruit peels are carbon sources that are successfully used in the hydrothermal synthesis of green CQDs [8]. CQDs with high quantum yields can be synthesized by using natural materials as carbon sources. Other compounds in such natural resources are included in CQDs during hydrothermal synthesis, such as phosphorus (P), nitrogen (N), and sulfur (S). It provides the spontaneous addition of heteroatoms [9]. There are literature about green-synthesized CQDs using the hydrothermal method [10–19]. In this study, rosehip was preferred as the carbon source for green synthesis because it had S and P elements in high amounts in both the core and the mesocarp. Therefore, it was spontaneously provided as a heteroatom additive to the CQDs produced by the hydrothermal method. This is the first study to obtain RC-CQDs by using rosehip fruit as a carbon source. PCL is a green material used for various applications or in the design of biomaterials. It has increased the use of PCL in a wide variety of biodegradable and processable materials due to its superior rheological and viscoelastic properties over most of its aliphatic polyester counterparts. Moreover, the mechanical properties of PCL make it suitable for complementary medical applications in tissue engineering, e.g., wound dressing, childbirth control pills, and dentistry, as well as in the environmental, packaging, and food industries. It is currently used with biopolymers due to its interesting bio-friendly properties. The use of PCL in combination with its adaptive degradation kinetics and mechanical properties provides ease of forming and fabrication, providing suitable pore sizes for growth within the tissue [20]. PCL matrix materials have been limited in their use in structural applications due to their low glass transition temperature and elastic properties. Its elastic modulus is quite low compared to other biodegradable polymers such as polylactic acid (PLA) or polyhydroxybutyrate (PHB) [20]. PCL is very slow to degrade compared to other polyesters, and therefore, it is suitable for both long-term drug release and as a tissue scaffold [21]. PCL undergoes degradation under physiological conditions by the hydrolysis of ester bonds. However, the hydrolytic degradation of hydrophobic PCL takes a long time in vivo [22]. For this reason, in some cases, PCL derivatives have also been produced for degradation triggered by H_2O_2 at physiological hydrogen peroxide (H_2O_2) levels for the purpose of controlled degradation with reactive oxygen species (ROS) [23]. Reactive oxygen species (ROS) are divided into two categories: free radicals and non-radical ROS. While non-radical ROS like singlet oxygen (1 O_2) and hydrogen peroxide (H_2O_2) do not have unpaired electrons, free radicals like superoxide (O_2), hydroxyl (OH%), and nitric oxide (NO%) have [24,25]. In this study, the slow degradation characteristic of PCL was initially followed, then accelerated H_2O_2-triggered degradation tests were performed using higher concentrations of H_2O_2 (1–10 mM), without using physiological H_2O_2 levels (50–100 μM). These degradation tests showed comparable degradation behavior in a short time of PCL nanocomposite films instead of the long-term physiological hydrolysis behavior. There are various studies on the behavior of biodegradable polymers at physiological H_2O_2 levels [26]. Components such as pine cone particles [27] and graphene derivatives (graphene quantum dots) [28] have been reported in various studies to improve the mechanical properties of composites. However, to the best of our knowledge, studies on the mechanical properties of PCL/CQDs nanocomposites are limited. For example; polyglycerol sebacate/polycaprolactone/carbon quantum dots (PGS/PCL/CQDs) fiber scaffolds were produced by the electrospinning method by Rastegar et al. [29] and the structural, mechanical, and biological properties of these scaffolds were investigated. In another study by Ghorghi et al. [30] captopril-doped PCL-CQDs nanocomposite scaffolds were produced by electrospinning and their physical, chemical, biological, and mechanical properties were reported. Carbon quantum dot Polyacrylonitrile/Polycaprolactone nanocomposite membranes for heavy metal purification were produced by electrospinning by Mabborang et al. [31] and their adsorption behavior was investigated. However, studies on the combination of fluorescent properties with PCL composite films and their use in both tissue engineering and drug delivery systems have been of interest recently [32]. Various studies with different composites have been reported. For example, in a study, the performance of PLA composites obtained by CQDs and micro-extrusion in cell and scaffold imaging was evaluated [33]. In a

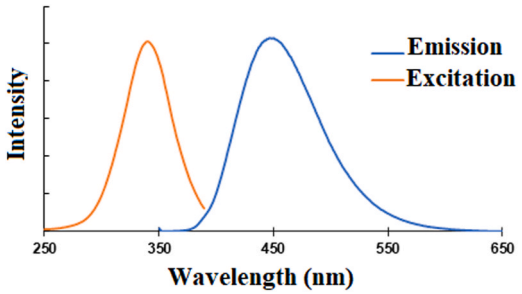

Fig. 1. Photoluminescence spectra of quinine sulfate in a 0.1 M H_2SO_4 solution selected as standard in the study.

recently published study, the imaging performance of a silk fibroin/-PLA/CQDs composite was evaluated [34]. To the best of our knowledge, there is no study on the properties of PCL nanocomposites, the variation of mechanical strength with filler ratio, or degradation behaviors. In this study, an optimization process was used to prepare RC-CQDs samples with rosehip fruit for the first time, and PCL/RC-CQDs samples synthesized under the conditions with the highest quantum yield were added to the PCL matrix with different wt% amounts. Samples of CA-CQDs were synthesized from the same wt% with citric acid as a familiar carbon source for comparison. The films containing both RC-CQDs and CA-CQDs were structurally characterized, and their mechanical and biodegradable properties were investigated.

2. Materials and methods

2.1. Materials

Rosehip (Rosa canina L.), which will be used as an economic carbon source in the study, was obtained from a local market in Turkey. Rosehip milled with a metal-blade miller was stored at +4 °C.

2.2. Preparation of CQDs samples

The hydrothermal method was used for the high quantum yield RC-CQDs, which can emit fluorescence from rosehip fruit. Ground rosehip was brewed with 160 ml of boiled distilled water and filtered with 1–2 μm filter paper. The filtrate was placed in a teflon autoclave with a volume of 200 ml and kept in an oven at the recommended experimental conditions (150.03 °C, 11.36 h, 74.45% occupancy rate) in order to obtain maximum efficiency after the optimization study with the surface response method [35,36]. Teflon was cooled to room temperature in an autoclave oven. The dark solution was heated at 6000 rpm for 30 min and centrifuged twice. A 0.22 μm cellulose ester membrane was used to eliminate large particles in the resulting suspension. The solutions were extracted with dichloromethane to remove the unreacted precursor molecules. The resulting filtrate was stored at +4 °C for characterization and film production.

Considering the Zhu et al. [37] in which citric acid is used as a known carbon source, 16.82 g of citric acid was dissolved in 160 ml of distilled water, then added to the Teflon autoclave and kept in an oven at 200 °C for 5 h. It decreased to room temperature and the dark yellow solution was filtered through a 0.22 μm cellulose ester membrane. The filtrate was stored at +4 °C for characterization and film production.

2.3. Production of PCL/CQDs films

The colloidal blending method was used to produce PCL films from RC-CQDs and CA-CQDs samples. The concentration of liquid-form RC-CQDs and CA-CQDs samples was determined by the liquid drying method for adding 0.3, 0.5, 1.2, 2.0, and 4.0 wt% to the polymer matrix. Concentration was calculated by Eq. (1) given below [38]. In the equation, C is the concentration, M_1 is the weight of the empty container, M_2 is the weight of the container in which the RC-CQDs and CA-CQDs were dried, and V is the volume of the RC-CQDs and CA-CQDs samples.

$$C = M_2 - M_{1/V} \quad (1)$$

The concentrations of RC-CQDs and CA-CQDs samples were calculated with this equation. According to the determined wt% values, the RC-CQDs and CA-CQDs contents were calculated according to 5 g PCL, and nanocomposite films were produced. They are encoded according to their wt% content. Such as PCL/RC-CQDs-0.3, which represents the nanocomposite film containing 0.3 wt% RC-CQDs.

PCL (5 g, 40 ml) was dissolved in tetrahydrofuran (THF) at 50 °C for the production of films. The solutions containing RC-CQDs and CA-CQDs in amounts corresponding to the wt% value were added to the PCL solution and mixed for 30 min with an ultrasonic homogenizer. The solutions mixed in a magnetic stirrer at 50 °C and 30 min and then it were poured into molds and dried in an oven at 50 °C for 4 h. The dried samples were removed from the mold and stored for characterization processes.

2.4. Characterization of CQDs samples and PCL/CQDs films

Rosehip powder was analyzed with an Axios model-Panalytical X-Ray Fluorescence Spectrometer (WD-XRF). The excitation-emission and absorption values to be used for quantum efficiency calculations of the CQDs samples were carried out with a fluorescence spectrophotometer (Agilent Cary Eclipse) and a UV–Vis–NIR spectrophotometer (Shimadzu UV-3600 Plus). The reference method was used to measure the quantum yield of the CQDs samples. In this study, quinine sulfate was used as a reference standard. Quinine sulfate was chosen as the reference standard because of the overlap in the excitation and emission ranges (270–400 nm (max. 351) excitation range and 380–590 nm (max. 450) emission range) with CQDs samples (Fig. 1). The standard quantum yield (QY_{QS}) of the solution of quinine sulfate prepared in 0.1 M H_2SO_4 is taken as 0.54. The fluorescent integral area and absorbance value (A) of CQDs and quinine sulfate solutions were measured at the same excitation wavelength. The fluorescent quantum yield of CQDs samples were calculated according to Eq. (2) given below [11].

$$QY_{CQD} = QY_{QS} \times \frac{I_{CQD}}{I_{QS}} \times \frac{A_{QS}}{A_{CQD}} \times \left(\frac{n_{CQD}}{n_{QS}}\right)^2 \times 100\% \quad (2)$$

QY_{CQDs} or QY_{QS} is the quantum yield, I is the area of the measured radiation spectrum, A is the absorbance value at the excitation wavelength, n is the diffraction coefficient of the solvent, and the subscript.

Perkin Elmer spectrum 100 FTIR was used for Fourier transform infrared spectroscopy (FTIR) analysis; EISS SUPRA 40 VP for scanning electron microscope (SEM) images; and Jeol 2100F 200 kV RTEM for transmission electron microscope (TEM) images of CQDs and PCL/CQDs films. The crystal structures of the films were determined by X-ray diffraction (XRD), and tensile tests using the Shimadzu AG-IC 100 kN tensile-compression tester and the Shimadzu HMV-2E microhardness tester were used for microhardness measurements. The microhardness values of all films were measured under a 25-gram load. The surface roughness of the samples was measured with the Mitutoyo Surtest SJ-400 profilometer. R_a: mean roughness; R_q: root mean square roughness; R_y: highest peak-to-trough parameter in evaluation length; and R_z: ten-point height (μm) obtained from the profiles. Biodegradation behaviors were investigated by exposure to 1–10 mM H_2O_2 with accelerated degradation tests at ± 1 °C of the selected films in phosphate buffer (PBS, pH = 7.2-@−37 ± 1 °C) and 0.154 M NaCl isotonic salt solutions (pH = 7.4-@−37).

The amount of degradation is calculated by Eq. (3) [30].

$$\text{Weight loss}(\%) = \frac{W_t - W_o}{W_0} \times 100 \quad (3)$$

Table 1
XRF analysis result of the rosehip fruit used in this study.

Analyte	Calibration status	Compound formula	Concentration	Unit	Calculation method	Status
Mg	Calibrated	Mg	0.347	%	Calculate	BgC;
Al	Calibrated	Al	0.036	%	Calculate	BgC;
Si	Calibrated	Si	0.122	%	Calculate	BgC;
P	Calibrated	P	2.878	%	Calculate	BgC;
S	Calibrated	S	1.235	%	Calculate	BgC;
Cl	Calibrated	Cl	1.434	%	Calculate	BgC;
K	Calibrated	K	50.149	%	Calculate	BgC;
Ca	Calibrated	Ca	41.996	%	Calculate	BgC;
Mn	Calibrated	Mn	0.588	%	Calculate	BgC;
Fe	Calibrated	Fe	0.390	%	Calculate	BgC;
Ni	Calibrated	Ni	0.220	%	Calculate	BgC;
Zn	Calibrated	Zn	0.129	%	Calculate	BgC;
Rb	Calibrated	Rb	0.123	%	Calculate	BgC;
Sr	Calibrated	Sr	0.354	%	Calculate	BgC;

Analyte	Calibration status	Compound formula	Concentration	Unit	Calculation method	Status
Mg	Calibrated	MgO	0.511	%	Calculate	BgC;
Al	Calibrated	Al2O3	0.060	%	Calculate	BgC;
Si	Calibrated	SiO2	0.230	%	Calculate	BgC;
P	Calibrated	P2O5	5.741	%	Calculate	BgC;
S	Calibrated	SO3	2.630	%	Calculate	BgC;
Cl	Calibrated	Cl	1.200	%	Calculate	BgC;
K	Calibrated	K2O	46.249	%	Calculate	BgC;
Ca	Calibrated	CaO	41.802	%	Calculate	BgC;
Mn	Calibrated	MnO	0.520	%	Calculate	BgC;
Fe	Calibrated	Fe2O3	0.382	%	Calculate	BgC;
Ni	Calibrated	NiO	0.191	%	Calculate	BgC;
Zn	Calibrated	ZnO	0.109	%	Calculate	BgC;
Rb	Calibrated	Rb2O	0.092	%	Calculate	BgC;
Sr	Calibrated	SrO	0.284	%	Calculate	BgC;

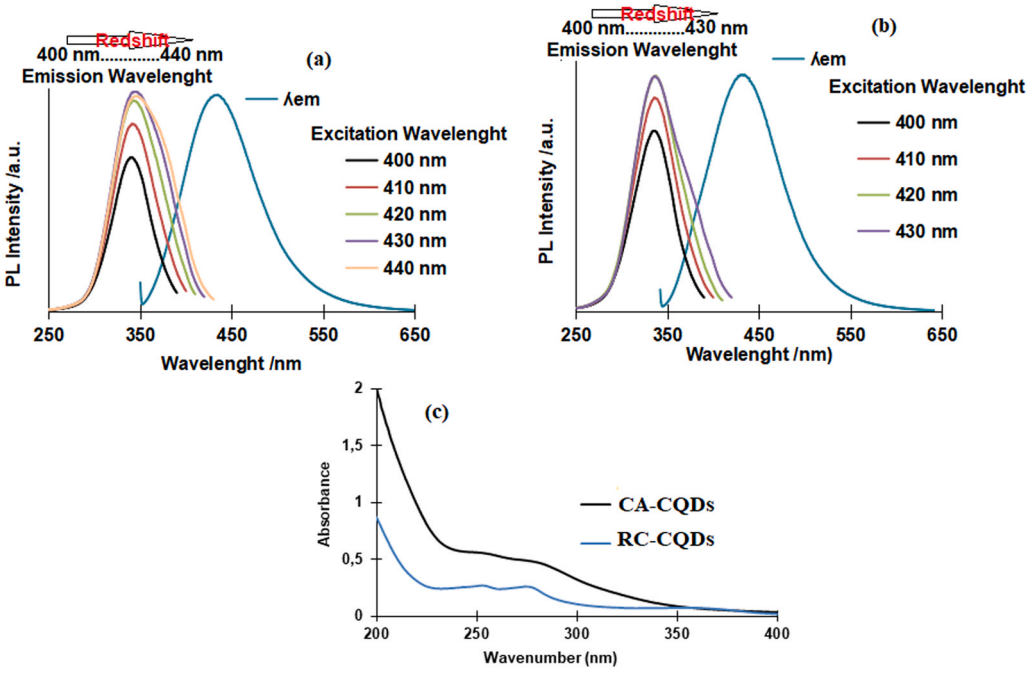

Fig. 2. (a) The corresponding emission spectra at different excitation wavelength, (b) fluorescence emission (blue line) spectra and (c) UV–Vis absorption spectra of RC-CQDs and CA-CQDs.

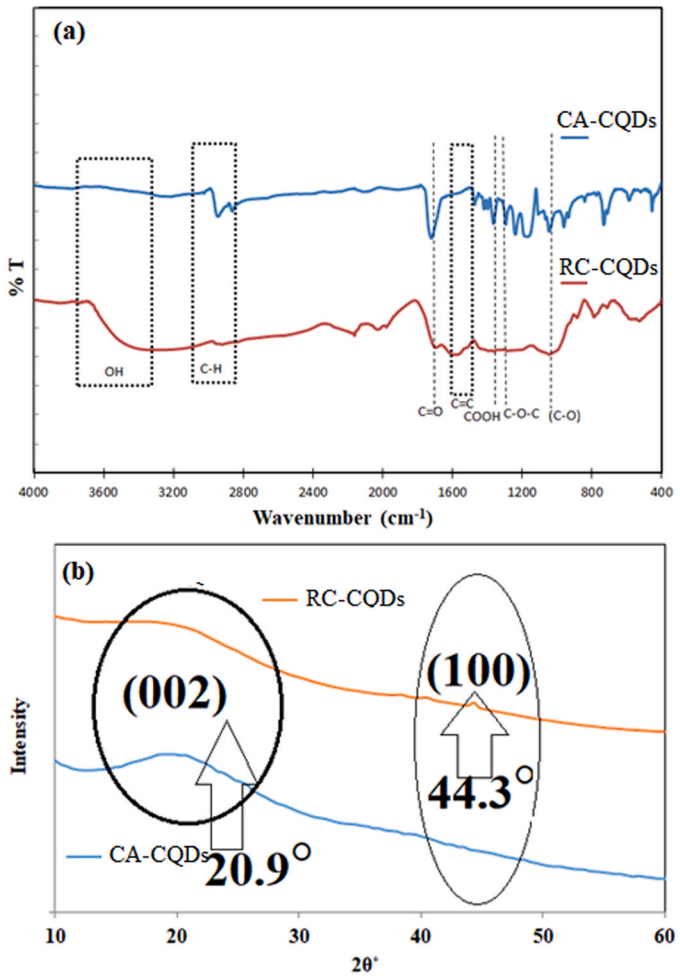

Fig. 3. (a) FTIR spectrum and (b) XRD pattern of the CQDs samples.

W_0: initial weight of samples W_t: the weight of the dried samples.

The masses (W_0) of the selected film samples were calculated and noted, and their degradation behavior without adding H_2O_2 for 41 days was observed for days 0 (1, 2, 3, 4 h), 1, 4, 9, 14, 19, and 41 days. Then, by adding 1 mM H_2O_2 to the same solutions on the 42nd day, the masses (Wt) of the samples removed from the solutions on the 42nd day (1, 3, 6 h), 43, 45, 47, and 51 days were calculated. Since the weight loss was not much, 10 mM more H_2O_2 was added to the same solution on the 52nd day, and the masses of the films were removed and dried on the 52nd day (1, 3, 6 h), 53, 54, and 57 days. It has been reported in the literature that the porous structure of PCL will cause some water absorption in the samples and thus change the weight measurement [39]. In this study, the samples removed from the solution were weighed after drying in an oven at 37 °C for 5 h before each weight measurement.

3. Results and discussion

3.1. XRF analysis of rosehip fruit

In this study, rosehip (Rosa canina L.) fruit was used as a carbon source and synthesized RC-CQDs by the hydrothermal method. The results of the XRF analysis of the powder obtained from both the mesocarp and the seed of rosehip are given in Table 1. It can be seen from Table 1 that S and P are higher in calcium (Ca) and potassium (K) content compared to other elements.

3.2. Fluorescence and UV–Vis–NIR spectroscopies analysis of RC-CQDs and CA-CQDs nanoparticules

Fig. 2(a-c) show corresponding emission spectra curves of RC-CQDs and CA-CQDs at different excitation wavelengths and fluorescence emission (blue line) spectra curves of CQDs nanoparticles, respectively. As shown in Fig. 2(a), the maximum emission appears at 435 nm when the excitation wavelength is 345 nm. It is observed that the emission spectra curves are nearly correlated with the excitation wavelengths from 400 to 440 nm, accompanied by the red shift (longer emission wavelength, λem) of the emission peaks. When the excitation wavelength is 337 nm, CA-CQDs show the strongest fluorescence at 431 nm. Besides, the fluorescence emission spectra exhibit a redshift with respect to the increment of the excitation wavelength ranging from 400 to 430 nm (Fig. 2(b)). Similar results for CQDs nanoparticles have also been reported previously [40] and these results indicate that CQDs show an excitation-dependent emission [41]. The ultraviolet-visible (UV–vis) absorption spectra of RC-CQDs and CA-CQDs nanoparticles are shown in Fig. 2(c). The UV–vis spectrum of RC-CQDs exhibited broad peaks at 260 and 280 nm, which were probably observed from the π-π* transition of the conjugated C═C bond. The absorption spectrum of CA-CQDs showed narrow peaks at 256 and 285 nm, which are attributed to the same transition of nanocarbon with RC-CQDs. Emission and UV wavelength values due to this excitation originating from CQDs have been reported [42–44]. But the peak intensity of CA-CQDs is lower than the spectrum of RC-CQDs. This suggested that RC-CQDs had stronger fluorescence than CA-CQDs. A quantum yield of 23.8% and 9.6% was obtained for the RC-CQDs and CA-CQDs, respectively. In this study, the CA-CQDs nanoparticle synthesized from citric acid was carried out in the same synthesis conditions without using ethylenediamine as in the study of Zhu et al. [37] to compare with the quantum yields of the RC-CQDs nanoparticle produced from rosehip without heteroatoms. The quantum yield was reported as 7.2% and the excitation wavelength was reported as 451 nm in the study of Zhu et al. [37] The quantum yield and the excitation wavelength results of this study were very close to those of Zhu et al. [37]. Therefore, the quantum yield result of RC-CQDs is reliable.

3.3. XRD and FTIR analysis of RC-CQDs and CA-CQDs nanoparticules

To identify the functional groups and surface structure of the as-synthesized CQDs nanoparticles, the FTIR spectra are measured, as shown in Fig. 3(a). All peaks of the CQDs obtained from different carbon

Table 2
The literature corresponding to the main functional groups for CQDs and the wavenumber values obtained from the FTIR analysis of this study [48,51–54].

CQDs (Literature)	Functional Groups	(This study)	RC-CQDs	CA-CQDs
3800–3300 cm^{-1}	OH		3853–3752–3317 cm^{-1}	3777–3251 cm^{-1}
2900–2800 cm^{-1}	C-H		2922–2836 cm^{-1}	2949–2863 cm^{-1}
1686 cm^{-1}	C═O		1690 cm^{-1}	1722 cm^{-1}
1650–1450 cm^{-1}	C═C		1579 cm^{-1}	1471 cm^{-1}
1370 cm^{-1}	COOH		1363 cm^{-1}	1365 cm^{-1}
1250 cm^{-1}	C–O–C		1281 cm^{-1}	1236 cm^{-1}
1066 cm^{-1}	(C–O)		1044 cm^{-1}	1042 cm^{-1}

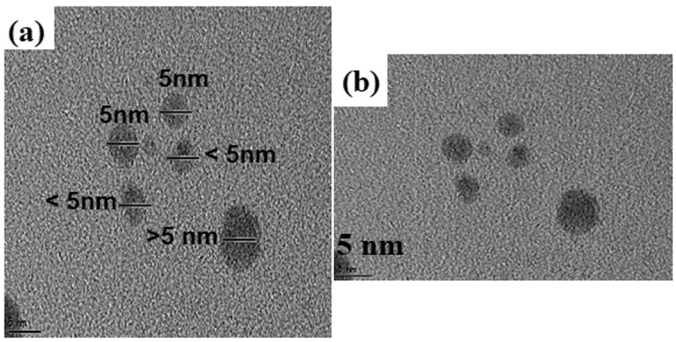

Fig. 4. The RTEM images of the (a) RC-CQDs and (b) CA-CQDs.

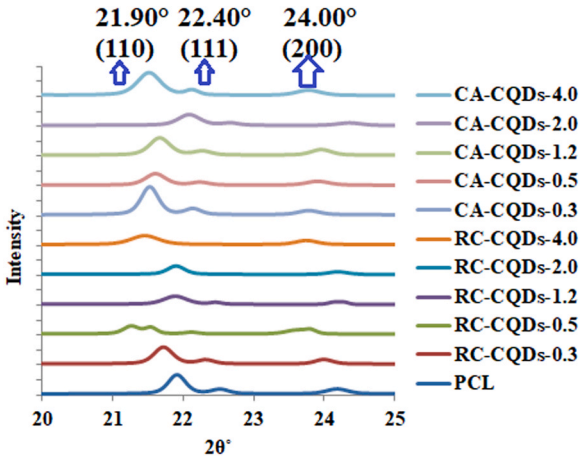

Fig. 5. XRD pattern of PCL and PCL/CQDs nanocomposite films.

sources in the literature and as-synthesized CQDs nanoparticles in this study are summarized in Table 2. As-showed broad peak in 3317 and weak peak at 3251 cm^{-1} in the FT-IR spectrum of RC-CQDs and CA-CQDs nanoparticules respectively, confirm hydroxyl group stretching vibrations. The Table 2 shows peaks at wavenumber 1690 and 1722 cm^{-1}, these peaks are ascribed to the carbonyl (C═O) stretching vibration. Fig. 3(a) indicates stronger peak at 1722 cm^{-1} associated with C═O stretching vibration of CA-CQDs groups than the peak of RC-CQDs nanoparticle. The results confirm that the both CQDs nanoparticules are functionalized with oxygen containing groups such as carboxyl, epoxyl, and hydroxyl [45]. The peaks in the wavenumber 1579 and 1471 cm^{-1} of RC-CQDs and CA-CQDs nanoparticules respectively, are related to the C═C in carbon dots, which is the origin of CQDs core [46]. The bands at 2922–2836 cm^{-1} and 2949–2863 cm^{-1} are ascribed to stretching of the C-H of RC-CQDs and CA-CQDs nanoparticules, respectively. Besides, there are several other characteristic peaks centered at 1363, 1281, and 1044 cm^{-1} that are ascribed to COOH stretching, C-O-C stretching, and C-O stretching of CQDs nanoparticules. The intensity of these group peaks is more severe in the CA sample. This means that the surfaces of CQDs nanoparticles were functionalized with oxygen-containing functional groups, a behavior similar to that reported in Ramezani et al. and Kumar et al. [47,48]. It is suggested that the formation of such oxygenic groups on the surface may be attributed to the effective interfacial interaction between polymer and quantum dots when applied in polymer nanocomposites. And also, it is clear that the more dominant presence of such functional groups on the surface of CA-CQDs will affect their hydrophilic properties. The crystal structure of the CQDs samples was evinced by the XRD pattern, shown in Fig. 3(b). The XRD profile showed peaks at 20.9° and 44.3°, which correspond to the (002) and (100) planes of the amorphous carbon phase and partial graphitization, respectively. In the literature, Wu et al. [49] and Yashwanth et al. [50] obtained close 2θ° values with this study, and they confirmed that the graphite structure was present in the carbon core of the carbon quantum dots.

3.4. RTEM analysis of RC-CQDs and CA-CQDs nanoparticules

The RTEM images of the CQDs samples are shown in Fig. 4(a–b). It was understood that the homogeneous shape and distribution of the RC-CQDs sample and the image of Fig. 4(a) exhibited a particle size of around 5 nm. However, the RTEM image of the CA-CQDs did not show a homogeneous size distribution, and it was greater than 5 nm (Fig. 4(b)). The amorphous nature of both CQDs samples was confirmed because they had no clear lattice fringes [55].

3.5. XRD analysis of PCL and PCL nanocomposite films

XRD patterns of PCL and PCL nanocomposite films are given in Fig. 5. The XRD pattern of PCL exhibited sharp characteristic peaks in two theta regions at 21.90° (110), 22.40° (111), and 24.00° (200), which correspond to the orthorhombic phase of the semicrystalline PCL matrix. The same patterns have been reported many times in the literature for PCL [55,56]. The nanocomposite films exhibited similar diffraction peaks with PCL, but it was observed that there were increases and decreases at the slide and intensity of diffraction peaks for all filler contents (Fig. 5). This change at diffraction peaks indicated good interaction between CQDs nanoparticles and PCL matrix. This result has also been reported in the studies of PCL [57,58]. In particular, it was determined that the peak corresponding to 22.5° (111) in PCL disappeared in the XRD patterns of the films containing 2.0% and 4.0% wt RC-CQDs. It was evidenced that RC-CQDs nanoparticules, especially at the highest contents, provided the interaction between the crystalline regions of the polymer, decomposed the semi-crystalline structure of PCL, and PCL/RC-CQDs films had an amorphous structure. The change in the crystal structure of PCL that contains different filler materials has been reported in some studies [59,60]. It was found that the addition of CA-CQDs to the PCL matrix did not affect the presence of crystal peaks, so the addition of CA-CQDs was not as effective on the crystal structure of PCL as the addition of RC-CQDs. As a result, PCL films exhibited an amorphous structure at high amounts of RC-CQDs, whereas the films obtained with the addition of CA-CQDs had a crystalline structure.

3.6. FTIR analysis of PCL and PCL nanocomposite films

The FTIR spectra of PCL and PCL nanocomposite films are shown in Fig. 6(a–b). The bands in the range 3800–3300 cm^{-1} were related to stretching vibrations of O-H groups in the spectrum of PCL [61]. The bands located at 2944 and 2865 cm^{-1} correspond to the asymmetric and symmetric stretching bands of -CH_2 groups, respectively. The band was observed at 2867 cm^{-1} due to stretching vibrations of the -CH_3 group. These bands were in accordance with the spectra of PCL [62]. The strong band at 1721 cm^{-1} which indicated the characteristic structure of PCL, was due to the C = O stretching vibration of the carbonyl group. The bands at 1470 cm^{-1}, 1365 cm^{-1}, 1239 cm^{-1}, 1163 cm^{-1} and 731 cm^{-1} were assigned as the C-H bending, C-H, asymmetric and symmetrical C-O-C stretch, and CH_2 bending stretching vibrations, respectively, and they were associated with the structure of PCL [63]. As seen from Fig. 6 (a), intensities of O-H group peaks increased and enlarged with the increase in RC-CQDs loading content, especially in PCL films containing 2.0 wt% and 4.0 RC-CQDs. In the FTIR spectra of CA-CQDs films in Fig. 6 (b), the bands of O-H stretching vibration at a wavenumber of 3393 cm^{-1} were widened and of low intensity, and a clear band appeared at CA-CQDs-4.0 film. Zhou et al. reported that the broadening of the peaks of -OH groups in polypropylene/graphene carbon quantum dot hybrids and this spectrum indicated hydrogen bond interactions between the filler and polymer matrix [64]. In the FTIR spectrum of PCL, the bands of CH_2 asymmetric-symmetric and CH_3 stretching vibrations,

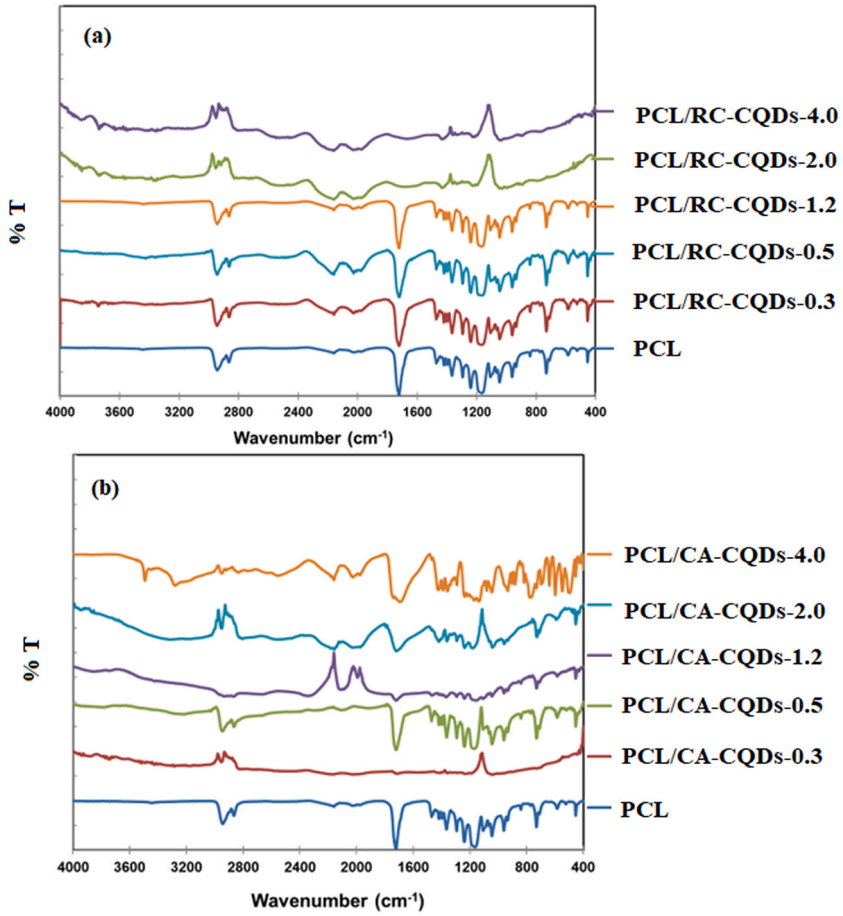

Fig. 6. FTIR spectrum of PCL, (a) RC-CQDs and (b) CA-CQDs nanocomposite films.

Fig. 7. PCL/CA-CQDs-4.0 film.

with the addition of RC-CQDs and CA-CQDs, shifted to larger wavenumbers between approximately 10 and 50 wavenumber values. In addition, the intensities of bands in the highest RC-CQDs and all CA-CQDs were significantly reduced. The shifts and decreases in intensity of FTIR bands were attributed to the mobility of polymer chains due to disruption of existing bonds, formation of new bonds, and interactions between the matrix and fillers [65,66]. In the FTIR spectrum of PCL, the bands corresponding to the C-O stretching vibration at a wavenumber of 1721 cm^{-1} were determined to shift larger wavenumbers at PCL/RC-CQDs-0.3, 0.5, and 1.2 films, and significant reductions in band intensities were observed at PCL/RC-CQDs-2.0 and 4.0. In the bands of the same wavenumber in films containing CA-CQDs, a significant reduction in intensity was observed in films containing 0.3% and 1.2% CQDs, while band broadening was observed in films containing 2.0%, 4.0%, and 0.5% CQDs. Especially in all films, the change observed in this band was due to polymer-CQD interactions and RC-CQDs and CA-CQDs successfully entering the polymer matrix at all weight percents. Jian et al. [67] observed the band of the C═O stretching vibration in the varying wavenumber values in polypropylene/CQD composites and attributed that to the interactions between CQD and polymer. Barros et al. [62] reported that the shift of the band observed at 1721 cm^{-1} in the FTIR spectrum of epoxy/PCL composites to a longer wavenumber of approximately 9 cm^{-1} in composites is due to secondary bonds formed between the carbonyl groups of PCL and the hydroxyl groups of epoxy. In this study, hydrogen bond formation occurred between the C═O group in the PCL structure and the C-H group in the CQD structure, which was confirmed by the decreases in intensity of both the CH and C═O group bands. Irimia et al. [68] presented FTIR findings that support the formation of new bonds between CQDs and the polymer matrix. The functional group bands of PCL corresponding to the wavenumbers of 1470, 1365, 1293, 1239, 1163, and 731 cm^{-1} showed shifts and serious intensity decreases in the FTIR bands at the highest RC-CQDs amounts and the lowest CA-CQDs amounts. According to FTIR analysis results, the maximum filler-matrix interaction was provided at PCL/RC-CQDs-2.0, PCL/RC-CQDs-4.0 and PCL/CA-CQDs-0.5. The XRD and FTIR analysis results of these films were expected to have significant effects on their mechanical properties.

3.7. Tensile test of PCL and PCL nanocomposite films

Tensile tests of PCL, PCL/RC-CQDs, and PCL/CA-CQDs nanocomposite films prepared according to the ASTM-E8 standard were

Table 3
The tensile test results of PCL and PCL nanocomposite films.

	Tensile strength (N/mm^2)	Elongation %	Yield strength (N/mm^2)
PCL	13.14	394	6.40
PCL/RC-CQDs-0.3	10.41	421	6.64
PCL/RC-CQDs-0.5	14.91	377	7.99
PCL/RC-CQDs-1.2	16.78	410	8.53
PCL/RC-CQDs-2.0	17.65	402	8.06
PCL/RC-CQDs-4.0	16.66	396	9.02
PCL/CA-CQDs-0.3	11.44	169	6.48
PCL/CA-CQDs-0.5	8.24	16.10	4.98
PCL/CA-CQDs-1.2	8.04	5.09	5.07
PCL/CA-CQDs-2.0	4.86	1.72	3.54
PCL/CA-CQDs-4.0	-	-	-

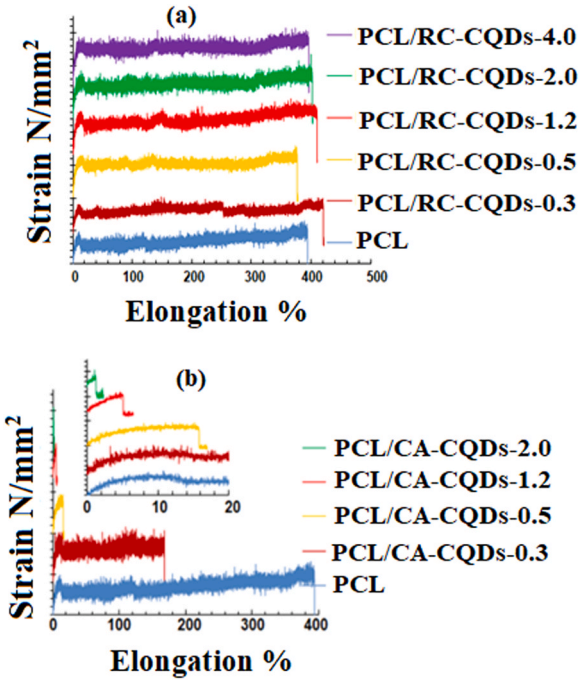

Fig. 8. Tensile test results of PCL, (a) RC-CQDs and (b) CA-CQDs nanocomposite films.

performed at room temperature. The tensile test of the PCL/CA-CQDs-4.0 film was not performed because the equipment had no data sensitivity for this film. The strength of this film was low enough that it could be broken by hand, as seen in Fig. 7.

Table 3 shows the results obtained from the tensile test of PCL and PCL nanocomposite films. It had been determined that the tensile strength, yield strength, and percentage elongation values given in the literature for PCL with the same molecular weight were compatible with the values obtained in this study [69,70]. The strength began to increase with the addition of RC-CQDs, particularly the tensile strength value of the 0.5% wt RC-CQDs added film, reaching the maximum tensile strength value with the addition of 2.0% wt. A 27.7% improvement was found in the tensile strength of the PCL/RC-CQDs-2.0 film compared to the polymer (Table 3). It was determined that the yield strength of the PCL/RC-CQDs-4.0 film at its maximum value increased by 40.9% compared to the PCL.

Tensile test results for PCL and PCL nanocomposite films are displayed in Fig. 8(a-b). Fig. 8(a) and Table 3 showed that the percentage elongation values of PCL/RC-CQDs films did not change significantly. An ideal result was obtained by increasing the strength values without disrupting the ductility of PCL with the addition of RC-CQDs. 1.2%, 2.0%, and 4.0% wt. values of the RC-CQDs were critical values that affected the mechanical properties of the films. The maximum tensile strength, the percentage elongation, and the yield strength values were observed in the PCL/RC-CQD-2.0, the PCL/RC-CQD-1.2, and the PCL/RC-CQD-4.0 films, respectively (Fig. 8(a)). Dhakal et al. [69] added palm fibers as fillers to the PCL matrix by the extrusion method and examined the mechanical properties of the samples. They attributed the increase in tensile strength to the interface interaction and the strength-enhancing properties of the filler. The decrease in % elongation values of samples was attributed to the ductile behavior of PCL and the filler, which caused a brittle structure. Jha et al. [27] produced pinecone/PCL biodegradable composites, and the brittle structure of the biodegradable composites was attributed to the weak matrix-filler interaction and the restriction of the polymer chain movements. In this study, the addition of RC-CQDs increased the strength of the structure of nanofilms, but the ductility of the nanofilm structure did not change. It was determined that the CQDs-PCL interaction was also provided, as reported in the FTIR analysis section. In particular, the formation of hydrogen bonds supported the increase in mechanical strength [71]. The mechanical properties of PCL/CA-CQDs films decreased with increasing CA-CQDs amount; the maximum values were determined at the lowest content (0.3% CA-CQDs), as shown in Table 3 and Fig. 8(b). The tensile test results of PCL/CA-CQDs film were compared with the results of PCL, and it was determined that only the yield strength value was preserved, the tensile strength value decreased by 14.8%, and the % elongation amount decreased by 133.1%.

Images of PCL and films during the tensile test are given in Fig. 9(a-c). As seen in Fig. 9(a) and (b), the films of PCL and PCL/RC-CQDs showed ductile behavior with necking and high elongation. In this study, the CA-CQDs sample produced using a known carbon source (citric acid) changed the structural properties of PCL, but it did not have an improved effect on the mechanical properties of PCL, contrary to the RC-CQDs synthesized from rosehip. Cobos et al. [72] formed nanocomposites with organic nanoparticles in a PCL matrix and reported that the ductile behavior of nanocomposites was related to the crystallinity of the structure. It was determined that the structure became brittle with the increase in crystallinity. Fig. 9(c) showed brittle fracture of PCL/CA-CQDs films. In this study, as a result of XRD analysis of the films, it was determined that the crystal structure of PCL deteriorated and the structure became more amorphous in the PCL/RC-CQDs films; however, a major change was not observed in the crystal structure of the PCL/CA-CQDs films.

3.8. Fracture surface analysis of PCL and PCL nanocomposite films

The PCL/RC-CQDs films with the lowest and highest tensile strength values were selected, and their fracture surfaces were examined in Fig. 10. PCL/RC-CQDs-0.3 film had a low tensile strength value but a higher % elongation value compared to PCL. More broken parts on the fracture surface and inward bending ends due to the high ductility of these ruptured parts were observed at Fig. 10. The effect of large fragments ruptured on the fracture surface and the wrinkled image tensile force on the PCL/RC-CQDs-2.0 film was an indicator of nanofilm strength (due to the contribution of RC-CQDs added to the matrix). At the same time, the same wrinkled appearance cannot be observed in PCL, which also supports this result. Fig. 10 shows the elemental distributions of carbon and oxygen determined by EDS mapping analysis of the fracture surfaces. The association of more oxygen groups, especially in the wrinkled areas, indicates the presence of RC-CQDs added to the

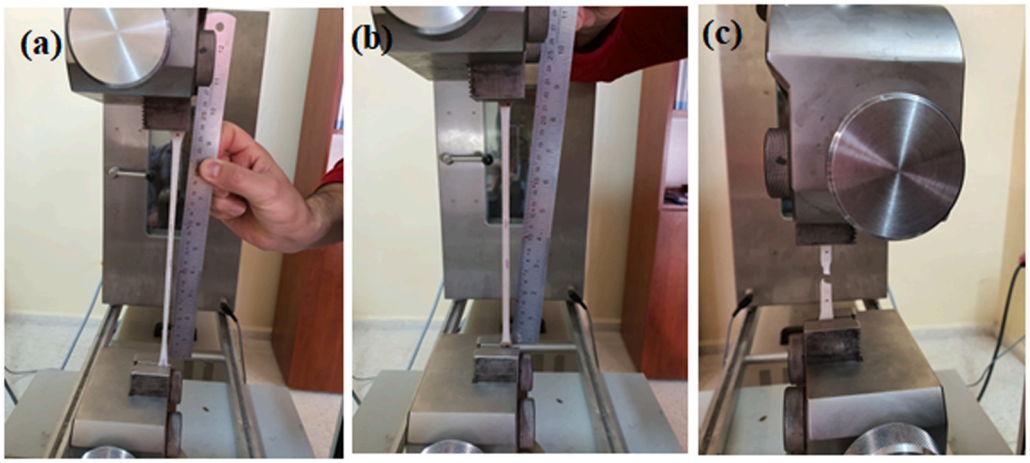

Fig. 9. Tensile test of (a) PCL, (b) PCL/RC-CQDs and (c) PCL/CA-CQDs films.

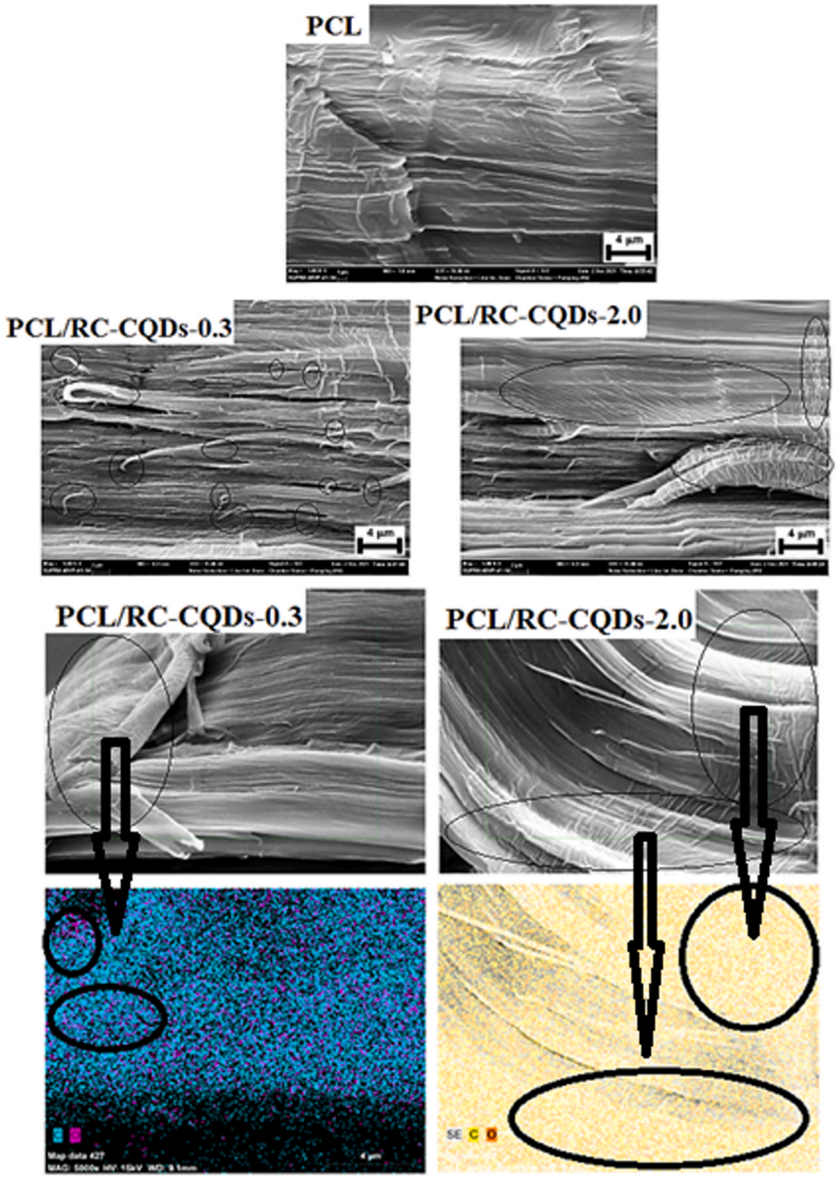

Fig. 10. Fracture surfaces and EDS mapping analysis of the fracture surfaces.

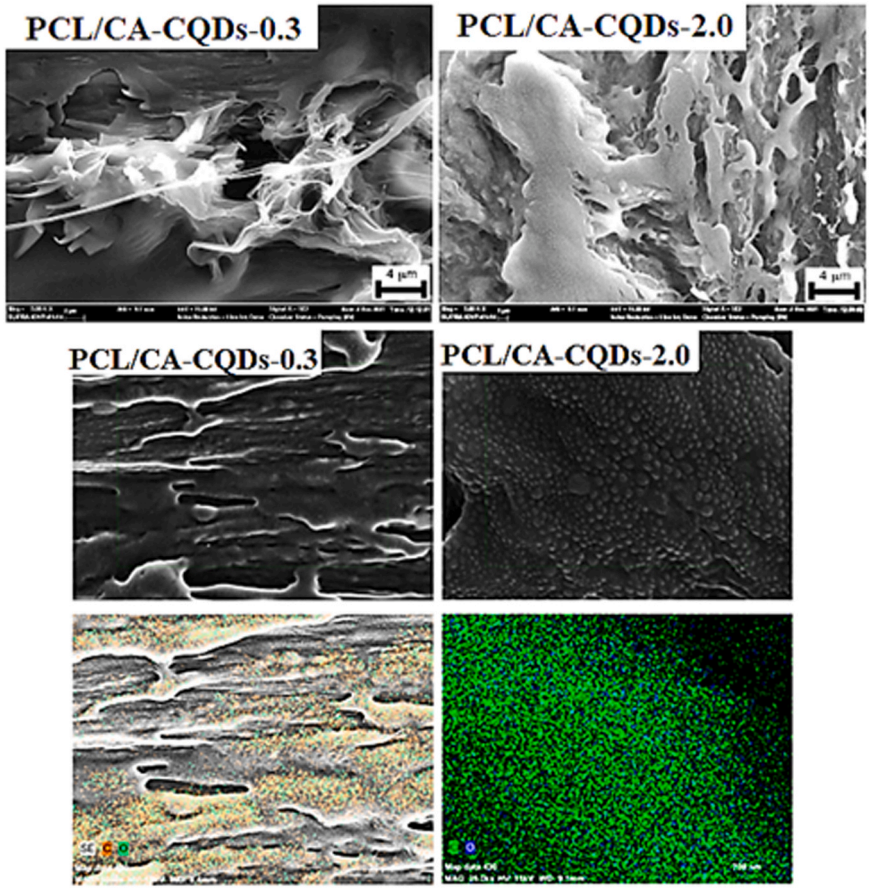

Fig. 11. Fracture surfaces and EDS mapping analysis of the fracture surfaces.

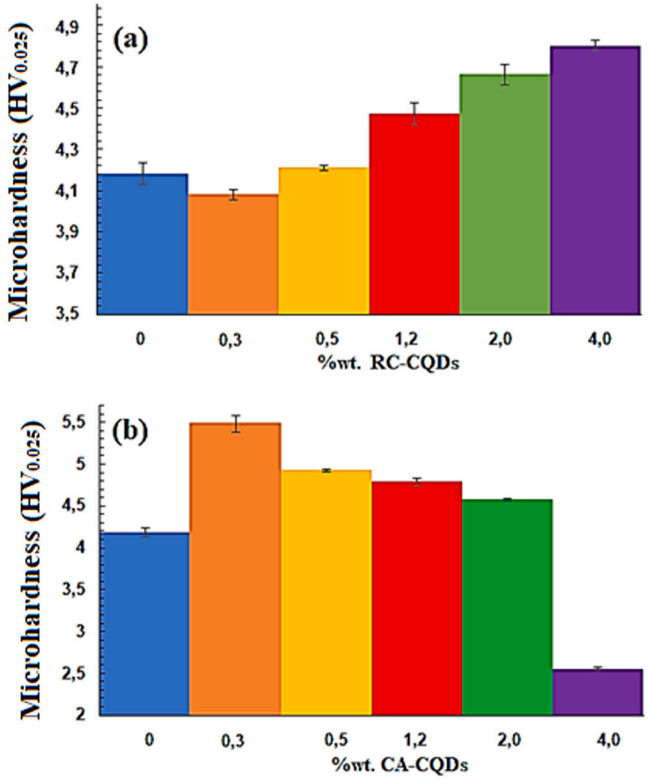

Fig. 12. The microhardness results of (a) PCL/RC-CQDs and (b) PCL/CA-CQDs films.

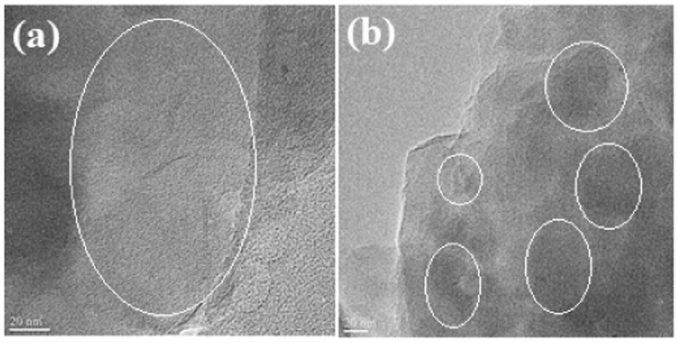

Fig. 13. The RTEM images of (a) PCL/RC-CQDs-2.0 and (b) PCL/CA-CQDs-2.0 films.

matrix.

Fig. 11 shows fractured surface images of PCL/CA-CQDs films with the lowest and highest tensile strength values compared to PCL. The irregular and rough fracture surface image of PCL/CA-CQDs-0.3 film was similar to the ductile fracture images reported in the literature [73]. The brittle structure of the PCL/CA-CQDs-2.0 film was revealed by the flat and smooth fractured surface image at Fig. 11. The brittle structure traces and the images obtained in this study were compatible with the fractured surface images in the literature [74]. The EDS mapping analysis of the same films, given in Fig. 11, showed the homogeneous distribution of CA-CQDs in the matrix.

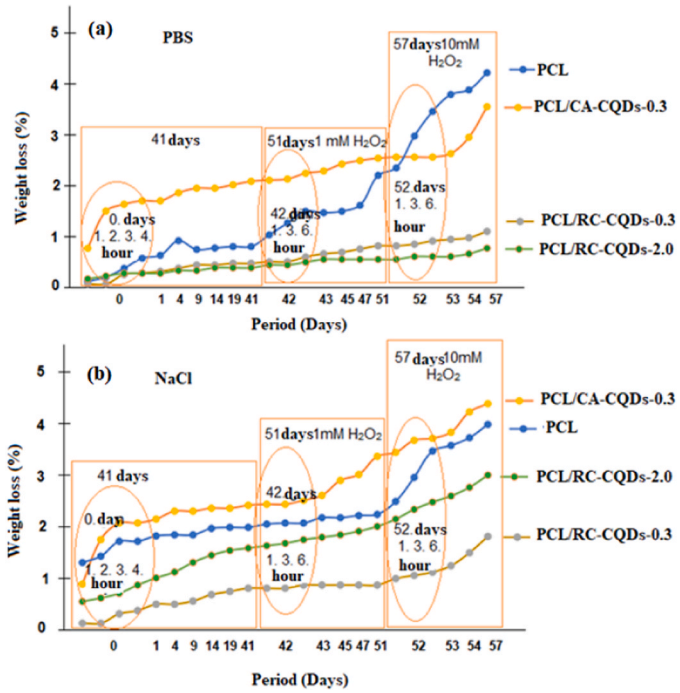

Fig. 14. 57-day weight loss of PCL, PCL/CA-CQDs-0.3, PCL/RC-CQDs-0.3 and PCL/RC-CQDs-2.0 films in (a) PBS solution and (b) NaCl solution.

3.9. Microhardness test results of PCL and PCL nanocomposite films

Fig. 12(a-b) shows the microhardness results measured under a 25-g load on the PCL and its films. The microhardness value of the PCL was determined at 4.18 $HV_{0.025}$. PCL/RC-CQDs-1.2, 2.0, and 4.0 films showed close results of the microhardness tests that were 4.47, 4.66, and 4.80, respectively (Fig. 12(a)). The tensile test results of the same films were also close to each other. PCL/RC-CQDs-4.0 film had the highest microhardness value; an increase in hardness value of 14.8% was observed compared to the PCL. The PCL/CA-CQDs-0.3 film gave the maximum microhardness value (5.48 $HV_{0.025}$) which was an increment of 22.5%, compared with PCL (4.18 $HV_{0.025}$) as shown in Fig. 12(a-b). The hardness values of PCL/CA-CQDs increased more than those of films containing RC-CQDs, which was attributed to the rearrangement of amorphous polymer chains rather than the crystal region of PCL [75]. The microhardness values showed an decrease with the increase in CA-CQDs content. The very low microhardness value of the PCL/CA-CQDs-4.0 film, in particular, confirmed that it had too low a strength for tensile testing. Kim et al. [76] attributed the increase in the hardness values of the polyurethane/carbon quantum dots (CQD) samples to physicochemical interactions such as hydrogen bond formation between the matrix and CQD. In this study, FTIR analysis results showed that the polymer-filler interactions of films containing both RC-CQDs and CA-CQDs (Fig. 6).

3.10. RTEM analysis of PCL nanocomposite films

The RTEM image of the PCL/RC-CQDs-2.0 and PCL/CA-CQDs-2.0 nanocomposites shown in Fig. 13(a-b) further confirms the structural and mechanical test results that the RC-CQDs were well-dispersed in the PCL matrix, but the CA-CQDs showed obvious aggregation or agglomeration in the matrix at 2.0%wt. CQDs samples with spherical morphology in the matrix showed aggregation in some regions in Fig. 13 (b). However, in the RTEM image of RC-CQDs example in Fig. 13(a), dark areas are generally less visible.

3.11. Biodegradability and surface roughness test results of PCL and PCL nanocomposite films

PCL/RC-CQDs-0.3, PCL/RC-CQDs-2.0 and PCL/CA-CQDs-0.3 were tested in PBS and 0.154 M NaCl solutions. Fig. 14(a-b) show the change in weight loss of PCL and its films during 57 days of degradation in PBS (pH = 7.2–37 °C) and 0.154 M NaCl solutions, respectively. It was clear that more weight loss occurred in the NaCl solution (Fig. 14(a-b)) from the 41-day degradation behavior of PCL before adding H_2O_2 to PBS and NaCl solutions. In the literature, the degradation behavior of PCL was investigated in the same (PBS and NaCl) solutions used in this study. Azevedo et al. [77] reported the 16-day degradation period of PCL in NaCl solution, and they observed a weight loss that ranged from 1.5% to

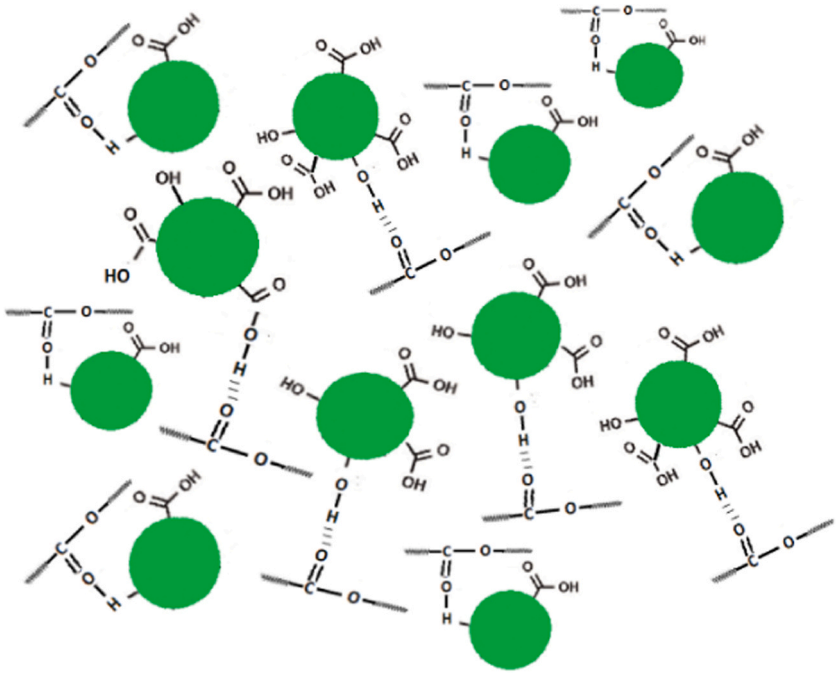

Fig. 15. Estimated mechanism of interaction between PCL-RC-CQDs.

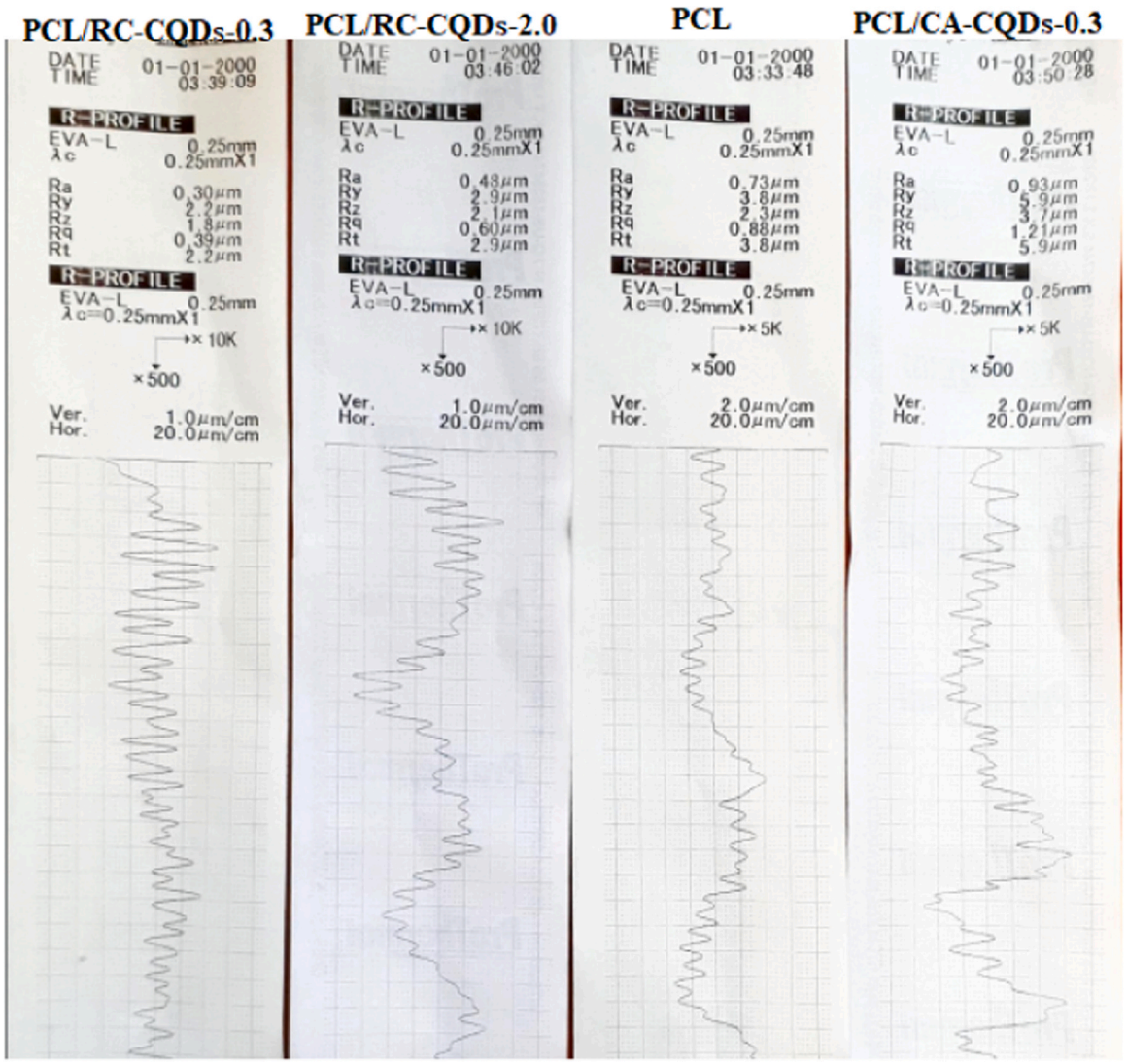

Fig. 16. Surface roughness values and profiles of biodegradability test samples.

2.0%. Díaz et al. [78], a weight loss of 0.2% in PBS solution was determined after a 16-week degradation period of PCL. In this study, a maximum weight loss of 1.9% was observed at the end of 41 days in NaCl solution and 0.7% in PBS solution. In general, the degradation rates of the polymers are affected by their structure, molecular weight, and other structural properties. PCL is hydrophobic; its degradation by hydrolysis is limited as it does not allow rapid water penetration. Although its mechanism is known to proceed by random hydrolytic chain scission of ester bonds, its degradation kinetics are relatively slower than other degradable polyesters such as PLLA or DLGA [78]. PCL tends to undergo amorphous phase reduction first and then further reduction in molecular size and crystalline phase before losing mass. The polymer tries to keep its structure after the chain degradation, it proceeds by cutting the chains in a mass after the degradation occurs [39]. At the end of 41 days, both films containing RC-CQDs in PBS solution had much lower weight loss results than the film containing PCL and CA-CQDs and were almost close to each other. In the NaCl solution, the film containing 0.3 wt% RC-CQDs gave the lowest weight loss results. Less degradation occurred as a result of the amorphous structures of the films with the addition of RC-CQDs. The low mechanical properties of PCL/CA-CQDs films were effective on the amount of degradation. Because of the semi-crystalline structure of the film, adding CA-CQDs caused the highest weight loss in both solutions. As can be seen from Fig. 14(a), the weight loss of PCL increased in PBS solution with the addition of 1 mM H_2O_2 on the 42nd day. In Fig. 14(b), a gradual increase in the weight loss of PCL/CA-CQDs-0.3 film was observed in the form of steps during the degradation process in the NaCl solution. The weight losses of the films containing RC-CQDs were lower in both solutions. The increasing amount of H_2O_2 after the 52nd day affected all the films significantly, and the degradation increased.

Among the physiologically present reactive oxygen species (ROS), superoxide radical anion (O_2-), hydroxyl radical ($^{\cdot}OH$), or hydrogen peroxide-derived radicals ($^{\cdot}OH$, $^{\cdot}OOH$, $H^{\cdot}$) have all been suggested as potential catalysts for PCL degradation. Degradation occurs by the radical withdrawing hydrogen from the polymer, followed by a series of cleavage events, and finally by combination with other radicals or by additional hydrogen removal. Such oxidative degradation primarily occurs within the amorphous regions of the polymer, and all radicals present in the environment do not participate in the degradation due to spontaneous recombination reactions with other active species. In general, hydrogen removal from PCL via radical interactions occurs at the α-carbon due to the electronegativity of the carbonyl oxygen. The absence of steric hindrance in this position and the resonance stabilization present in the first product (between α-carbon and carbonyl carbon and oxygen) support the reaction. In the mechanism, a hydrogen is cleaved from the α carbon following the reaction with oxygen to form a peroxy radical. This addition traps the radical on the polymer and can prevent its interaction with another radical, such as a hydrogen radical.

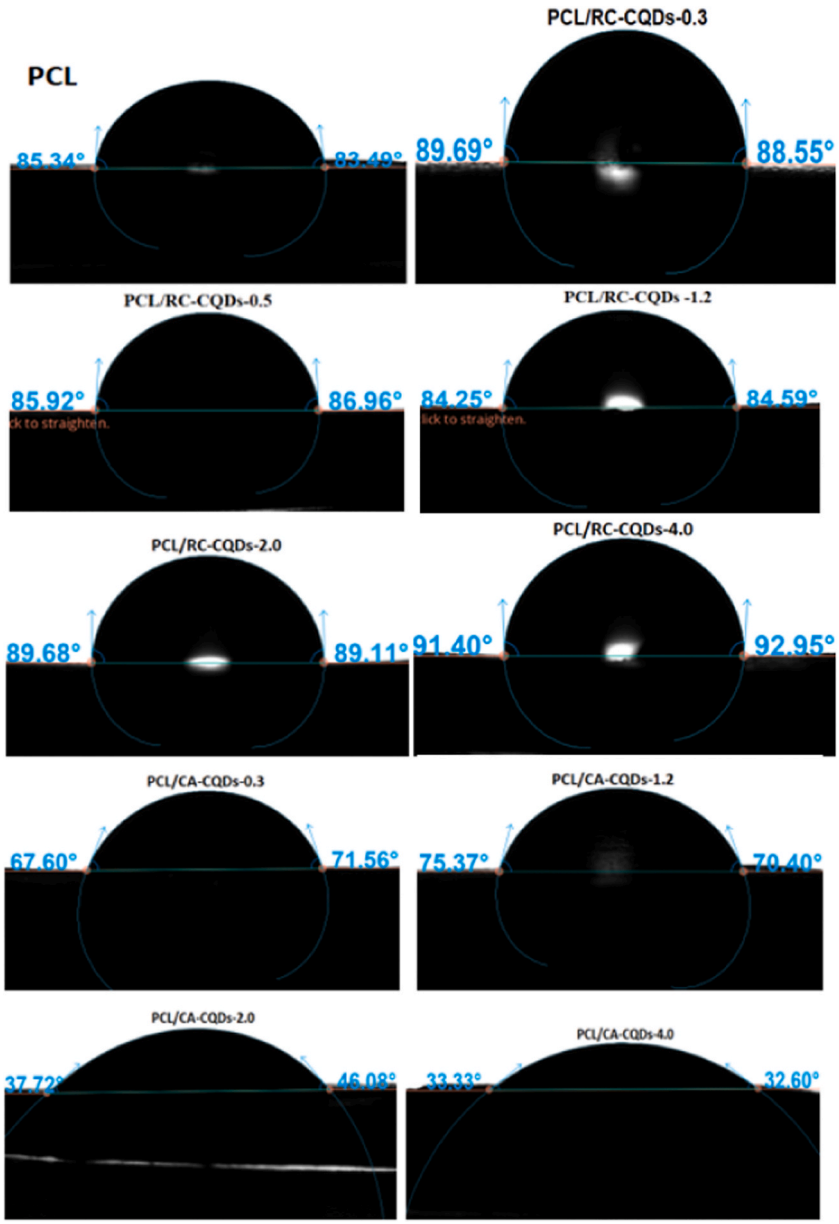

Fig. 17. Contact angle results of the films.

Alternatively, ester hydrolysis catalyzed by the superoxide radical anion (O_2·–) is possible via a nucleophilic attack to form carboxylic acid and alcohol products. These reactions basically produce a hydrolytic ester secession reaction, with the superoxide ion attacking the carbonyl carbon. The resulting hydroxy-end PCL (alcohol product) is produced in the first hydrolytic step after protonation (shown without a proton). The radical at the end of the peroxide-bound PCL then reacts with a superoxide radical, resulting in the release of a stable peroxide and O_2. The interaction with a hydroxide ion in the last step gives the carboxylate anion (carboxyl-terminated PCL after protonation) and dioxidanide (HOO–) products [79]. In this study, PCL/CA-CQDs-0.3 film showed the highest weight loss percentage in both PBS solution and NaCl solution due to its lower tensile strength value than PCL. This showed that the degradation occurred through two different degradation mechanisms, directly and indirectly. The degradation mechanism of PCL/CA-CQDs-0.3 film was similar to the degradation mechanism of PCL because both had a semi-crystalline structure. The same degradation mechanism was observed not only in PCL/CA-CQDs-0.3 but also in all films containing CA-CQDs. After adding 10Mm H_2O_2 on the 52nd day, the film containing CA-CQDs in the PBS solution showed lower weight loss values than PCL and was close to the solution containing NaCl. It was determined that at the beginning of the degradation process, the amorphous regions decomposed more quickly and then the crystalline regions decomposed more slowly. This is evident from the similarities with the degradation mechanism of PCL. The RC-CQDs-PCL interaction mechanism showed that PCL/RC-CQDs films undergo some degradation only through the indirect degradation mechanism. The amorphous structure of PCL/RC-CQDs films and the hydrogen bond interaction between the carbonyl group of PCL and the hydroxyl groups of RC-CQDs determined from the XRD and FTIR analysis results of the films, respectively, were shown in Fig. 15. It is likely that hydrogen bonds and amorphous structure may create a steric hindrance and resonance stabilization will be hindered by intervening RC-CQDs. Therefore, it is thought that the indirect mechanism between α-carbon and carbonyl carbon and oxygen does not occur; even if it did, there would be no steric hindrance, and resonance stabilization could occur to some extent in existing configurations. In the direct mechanism, a hydrolytic ester cleavage reaction occurs by attacking the carbonyl carbon

of the superoxide ion. However, in this study, the hydrogen bond formed between carbonyl groups and CQDs may prevent this attack. Therefore, films containing RC-CQDs exposed much less biodegradation than PCL. In the literature, the PCL/hydroxyapatite composite had less degradation than the PCL, which was attributed to better polymer-additive interfacial interaction and a more hydraulically stable composite structure [77]. In this study, the presence of polymer-fill interactions was determined by improvements in mechanical properties. Díaz et al. [78], reported that the increase in porosity of the structure increases the biodegradation of PCL/hydroxyapatite composites. In this study, information about porosity was obtained by measuring the surface roughness of films and PCL. The surface roughness values and profiles obtained from the surface roughness test were given in Fig. 16. As can be seen from Fig. 16, the highest mean square root roughness (Rq) value was detected in PCL/CA-CQDs-0.3 film, followed by PCL and the lowest Rq value in films containing RC-CQDs. It has been determined that these results were compatible with the degradation results of the literature and films.

3.12. Contact angle test results of PCL and PCL nanocomposite films

To compare the contact angle results of the films with the surface roughness results, the influence of RC-CQDs and CA-CQDs on the surface properties of PCL/RC-CQDs and PCL/CA-CQDs films was evaluated with contact angle tests, as shown in Fig. 17. Because it is known that the contact angle decreases as the surface becomes rough [80]. The PCL/RC-CQDs-2.0 (89.39°) and PCL/RC-CQDs-4.0 (97.17°) demonstrated a higher contact angle value as compared to the PCL (84.41°). Further increases in the amount of CA-CQDs led to a continuous reduction in contact angle values because the PCL/CA-CQDs films became hydrophilic and had a rough surface. Water contact angles become much lower, which indicates the surface hydrophilicity of the biodegradable polymers [81], RC-CQDs made PCL films more hydrophobic. This result confirmed the highest biodegradability test results of the PCL/CA-CQDs-0.3 film.

4. Conclusion

RC-CQDs and CA-CQDs samples were synthesized from rosehip fruit and citric acid by the hydrothermal method. PCL/RC-CQDs and PCL/CA-CQDs nanocomposite films were produced by adding RC-CQDs and CA-CQDs samples into the PCL matrix by the colloidal mixing method. The structural, mechanical, and biodegradable properties of these films were examined. The fluorescence quantum yield was determined to be 23.8% for RC-CQDs and 9.6% for CA-CQDs. FTIR analysis of CQDs samples showed the presence of oxygenated groups on their surface. XRD analysis results confirmed the amorphous carbon phase and partial graphitization of both CQDs samples. The homogeneous shape and distribution of the RC-CQDs sample were observed from the RTEM image, with a particle size of around 5 nm. According to XRD analysis, it was the more dominant amorphous structure of PCL/RC-CQDs films, but the semi-crystalline structure of polymer did not change with the fill of CA-CQDs. The shifts of bands in the FTIR spectrum of all films confirmed the existence of interactions between CQDs and PCL. The ductility of the polymer structure did not change; the strength increased with the addition of RC-CQDs, but the structure became brittle with the addition of CA-CQDs. The maximum increases in the microhardness value were detected in the films containing the highest RC-CQDs and the lowest CA-CQDs. The results of the biodegradability test performed in two different solutions showed that the percentage weight loss values were the lowest in the films containing RC-CQDs and the highest in the films containing CA-CQDs. The biodegradability behavior of the PCL/CQDs films is explained by the semi-crystalline structure, high surface roughness, and low contact angle of the PCL/CA-CQDs films and the amorphous structure, low surface roughness, and high contact angle values of the PCL/RC-CQDs films.

CRediT authorship contribution statement

F. Mindivan: Conceptualization, Investigation, Writing – original draft, Resources, Funding acquisition. **M. Göktaş:** Conceptualization, Investigation, Writing – original draft, Writing – review & editing, Resources, Supervision.

Declaration of Competing Interest

The authors declare that they have no known competing financial interests or personal relationships that could have appeared to influence the work reported in this paper.

Data availability

Data will be made available on request.

Acknowledgments

The authors thank the financial support of the research foundation (Project no: 2021-02. BSEÜ.01-03) of Bilecik Seyh Edebali University and TUBITAK-120M872 (The Scientific and Technological Research Council of Turkey).

References

[1] Y. Zhao, Y. Zhang, X. Liu, et al., Novel carbon quantum dots from egg yolk oil and their haemostatic effects, Sci. Rep. 7 (2017), 4452, https://doi.org/10.1038/s41598-017-04073-1.
[2] K. Kumar, A. Kumar, S. Devi, S. Tyagi, D. Kaur, Relevant photovoltaic effect in N-doped CQDs/MoS_2 (0D/2D) quantum dimensional heterostructure, Ceram. Int. 48 (10) (2022) 14107–14116, https://doi.org/10.1016/j.ceramint.2022.01.296.
[3] N. Jamaludin, T.L. Tan, A.S.K. Zaman, A.R. Sadrolhosseini, S.A. Rashid, Acid-free hydrothermal-extraction and molecular structure of carbon quantum dots derived from empty fruit bunch biochar, Materials 13 (15) (2020) 3356, https://doi.org/10.3390/ma13153356.
[4] K.L. Wong, J.C.G. Bünzli, P.A. Tanner, Quantum yield and brightness, J. Lumin. 224 (2020), 117256, https://doi.org/10.1016/j.jlumin.2020.117256.
[5] F. Abdolrezaei, M. Sabet, In situ green synthesis of highly fluorescent Fe_2O_3@CQD/graphene oxide using hard pistachio shells via the hydrothermal-assisted ball milling method, Luminescence 35 (5) (2020) 684–693, https://doi.org/10.1002/bio.3773.
[6] T. Arumugham, M. Alagumuthu, R.G. Amimodu, S. Munusamy, S.K. Iyer, A sustainable synthesis of green carbon quantum dot (CQD) from Catharanthus roseus (white flowering plant) leaves and investigation of its dual fluorescence responsive behavior in multi-ion detection and biological applications, SM&T 23 (2020), e00138, https://doi.org/10.1016/j.susmat.2019.e00138.
[7] X. Guo, H. Zhang, H. Sun, M.O. Tade, S. Wang, Green synthesis of carbon quantum dots for sensitized solar cells, ChemPhotoChem 1 (4) (2017) 116–119, https://doi.org/10.1002/cptc.201600038.
[8] J. Shen, S. Shang, X. Chen, D. Wang, Y. Cai, Facile synthesis of fluorescence carbon dots from sweet potato for Fe^{3+} sensing and cell imaging, Mater. Sci. Eng. C 76 (2017) 856–864, https://doi.org/10.1016/j.msec.2017.03.178.
[9] W. Lu, X. Qin, A.M. Asiri, A.O. Al-Youbi, X. Sun, Green synthesis of carbon nanodots as an effective fluorescent probe for sensitive and selective detection of mercury (II) ions, J. Nanopart. Res. 15 (1) (2012), 1344, https://doi.org/10.1007/s11051-012-1344-0.
[10] V. Wongso, N.S. Sambudi, S.S. Isnaeni, The effect of hydrothermal conditions on photoluminescence properties of rice husk-derived silica-carbon quantum dots for methylene blue degradation, Biomass Convers. Biorefin. 11 (2021) 2641–2654, https://doi.org/10.1007/s13399-020-00662-9.
[11] H. Yang, B. Zhou, Y. Zhang, H. Liu, Y. Liu, Y. He, S. Xia, Valorization of expired passion fruit shell by hydrothermal conversion into carbon quantum dot: physical and optical properties, Waste Biomass Valoriz. 12 (2021) 2109–2117, https://doi.org/10.1007/s12649-020-01132-z.
[12] N. Irmania, K. Dehvari, G. Gedda, P.-J. Tseng, J.-Y. Chang, Manganese-doped green tea-derived carbon quantum dots as a targeted dual imaging and photodynamic therapy platform, J. Biomed. Mater. Res. Part B Appl. Biomater. 108B (2020) 1616–1625, https://doi.org/10.1002/jbm.b.34508.
[13] A. Tadesse, M. Hagos, D. Ramadevi, K. Basavaiah, N. Belachew, Fluorescent-nitrogen-doped carbon quantum dots derived from citrus lemon juice: green synthesis, mercury(II) ion sensing, and live cell imaging, ACS Omega 5 (2020) 3889–3898, https://doi.org/10.1021/acsomega.9b03175.
[14] N. Chaudhary, P.K. Gupta, S. Eremin, P.R. Solanki, One-step green approach to synthesize highly fluorescent carbon quantum dots from banana juice for selective detection of copper ions, J. Environ. Chem. Eng. 8 (2020), 103720, https://doi.org/10.1016/j.jece.2020.103720.

[15] P. Surendran, A. Lakshmanan, G. Vinitha, G. Ramalingam, P. Rameshkumar, Facile preparation of high fluorescent carbon quantum dots from orange waste peels for nonlinear optical applications, Luminescence 35 (2020) 196–202, https://doi.org/10.1002/bio.3713.
[16] C. Dias, N.P. Vasimalai, M. Sarria, I. Pinheiro, V. Vilas-Boas, J. Peixoto, B. Espina, Biocompatibility and bioimaging potential of fruit-based carbon dots, Nanomaterials 9 (2019) 199, https://doi.org/10.3390/nano9020199.
[17] K. Rajendran, G. Rajendran, J. Kasthuri, K. Kathiravan, N. Rajendiran, Sweet corn (Zea mays L. var. rugosa) derived fluorescent carbon quantum dots for selective detection of hydrogen sulfide and bioimaging applications, Chem. Sel. 4 (46) (2019) 13668–13676, https://doi.org/10.1002/slct.201903385.
[18] E. Arkan, A. Barati, M. Rahmanpanah, L. Hosseinzadeh, S. Moradi, M. Hajialyani, Green synthesis of carbon dots derived from walnut oil and an investigation of their cytotoxic and apoptogenic activities toward cancer cells, Adv. Pharm. Bull. 8 (1) (2018) 149–155, https://doi.org/10.15171/apb.2018.018.
[19] N. Vasimalai, V. Vilas-Boas, J. Gallo, M.F. Cerqueira, M. Menendez-Miranda, J. M. Costa-Fernandez, L. Dieguez, B. Espina, M.T. Fernandez-Arguelles, Green synthesis of fluorescent carbon dots from spices for in vitro imaging and tumour cell growth inhibition, Beilstein J. Nanotechnol. 9 (2018) 530–544, https://doi.org/10.3762/bjnano.9.51.
[20] V. Guarino, G. Gentile, L. Sorrentino, L. Ambrosio, Polycaprolactone: synthesis, properties, and applications, Encycl. Polym. Sci. Technol. (2017) 1–2, https://doi.org/10.1002/0471440264.pst658.
[21] K. Miladi, D. Ibraheem, M. Iqbal, S. Sfar, H. Fessi, A. Elaissari, Particles from preformed polymers as carriers for drug delivery, EXCLI J. 13 (2014) 28–57, https://doi.org/10.17877/DE290R-15560.
[22] M.A. Woodruff, D.W. Hutmacher, The return of a forgotten polymer-polycaprolactone in the 21st century, Prog. Polym. Sci. 35 (10) (2010) 1217–1256, https://doi.org/10.1016/j.progpolymsci.2010.04.002.
[23] P.-H. Hsu, C. Arboleda, A. Stubelius, L.-W. Li, J. Olejniczaka, A. Almutairi, Highly responsive and rapid hydrogen peroxidetriggered degradation of polycaprolactone nanoparticles, Biomater. Sci. 8 (2020) 2394–2397, https://doi.org/10.1039/C9BM02019E.
[24] Z.M. Marković, S.P. Jovanović, P.Z. Mašković, M.M. Mojsin, M.J. Stevanović, M. Danko, B.M.T. Marković, Graphene oxide size and structure pro-oxidant and antioxidant activity and photoinduced cytotoxicity relation on three cancer cell lines, J. Photochem. Photobiol. B 200 (2019), 111647, https://doi.org/10.1016/j.jphotobiol.2019.111647.
[25] Z.M. Marković, M. Kováčová, S.R. Jeremić, Š. Nagy, D.D. Milivojević, P. Kubat, B. M. Todorović Marković, et al., Highly efficient antibacterial polymer composites based on hydrophobic riboflavin carbon polymerized dots, Nanomaterials 12 (22) (2022) 4070, https://doi.org/10.3390/nano12224070.
[26] C. Gracia Lux, S. Joshi-Barr, T. Nguyen, E. Mahmoud, E. Schopf, N. Fomina, A. Almutairi, Biocompatible polymeric nanoparticles degrade and release cargo in response to biologically relevant levels of hydrogen peroxide, J. Am. Chem. Soc. 134 (2012) 15758–15764, https://doi.org/10.1021/ja303372u.
[27] K. Jha, Y.K. Tyagi, A.S. Yadav, Mechanical and thermal behaviour of biodegradable composites based on polycaprolactone with pine cone particle, Sådhanå 43 (2018), 135, https://doi.org/10.1007/s12046-018-0822-1.
[28] M. Bagheri, A. Mahmoodzadeh, Polycaprolactone/graphene nanocomposites: synthesis, characterization and mechanical properties of electrospun nanofbers, J. Inorg. Organomet. Polym. Mater. 30 (2020) 1566–1577, https://doi.org/10.1007/s10904-019-01340-8.
[29] S. Rastegar, M. Mehdikhani, A. Bigham, E. Poorazizi, M. Rafienia, Poly glycerol sebacate/ polycaprolactone/ carbon quantum dots fibrous scaffold as a multifunctional platform for cardiac tissue engineering, Mater. Chem. Phys. 266 (2021), 124543, https://doi.org/10.1016/j.matchemphys.2021.12454.
[30] M. Ghorghi, M. Rafienia, V. Nasirian, F.S. Bitaraf, A.M. Gharravi, A. Zarrabi, Electrospun captopril-loaded PCL-carbon quantum dots nanocomposite scaffold: Fabrication, characterization, and in vitro studies, Polym. Adv. Technol. 31 (2020) 3302–3315, https://doi.org/10.1002/pat.5054.
[31] C.M.P. Mabborang, J.N.B. Padrigo, G.M. Quiachon, P.A.N. de Yro, Synthesis and characterization of electrospun carbon quantum dots – polyacrylonitrile/ polycaprolactone composite nanofiber membranes for copper (II) adsorption, Key Eng. Mater. 878 (2021) 3–8, https://doi.org/10.4028/www.scientific.net/KEM.878.3.
[32] D. Mondal, M. Griffith, S. Venkatraman, Polycaprolactone based biomaterials for tissue engineering and drug delivery: current scenario and challenges, Int. J. Polym. Mater. Polym. Biomater. 65 (5) (2016) 255–265, https://doi.org/10.1080/00914037.2015.1103241.
[33] A. Dehghani, S.M. Ardekani, M. Hassan, V.G. Gomes, Collagen derived carbon quantum dots for cell imaging in 3D scaffolds via two-photon spectroscopy, Carbon 131 (2018) 238–245, https://doi.org/10.1016/j.carbon.2018.02.006.
[34] C. Yan, Y. Ren, X. Sun, L. Jin, X. Liu, H. Chen, K. Wang, M. Yu, Y. Zhao, Photoluminescent functionalized carbon quantum dots loaded electroactive Silk fibroin/PLA nanofibrous bioactive scaffolds for cardiac tissue engineering, J. Photochem. Photobiol. B Biol. 202 (2020), 111680, https://doi.org/10.1016/j.jphotobiol.2019.111680.
[35] F. Mindivan, Investigation of the Effect of Loading Ratio on the Mechanical Properties and Degradation Process of Green Synthesized Carbon Quantum Dot-biodegradable Poly (Caprolactone) Nanocomposite Films, The Scientific and Technological Research Council of Turkey (TUBITAK) Project No: 120M872.
[36] F. Mindivan, S. Makta, M.O. Caglayan, Statıstıcal optımızatıon of experımental parameters for synthesıs of carbon nanodots by response surface methodology, in: Proceedings of the 6nd International Conference on Material Science and Technology in Cappadocia (IMSTEC'21), Cappadocia, Turkey, November 26–27–28 2021.
[37] S. Zhu, Q. Meng, L. Wang, J. Zhang, Y. Song, H. Jin, K. Zhang, H. Sun, H. Wang, B. Yang, Highly photoluminescent carbon dots for multicolor patterning, sensors, and bioimaging, Angew. Chem. Int. Ed. 52 (2013) 3953–3957, https://doi.org/10.1002/anie.201300519.
[38] L. Xu, Y. Li, S. Gao, Y. Niu, H. Liu, C. Mei, J. Cai, C. Xu, Preparation and properties of cyanobacteria-based carbon quantum dots/polyvinyl alcohol/ nanocellulose composite, Polymers 12 (5) (2020) 1143, https://doi.org/10.3390/polym12051143.
[39] C.L. Salgado, E.M. Sanchez, C.A. Zavaglia, P.L. Granja, Biocompatibility and biodegradation of polycaprolactone-sebacic acid blended gels, J. Biomed. Mater. Res A 100 (1) (2012) 243–251, https://doi.org/10.1002/jbm.a.33272.
[40] C. Zhu, J. Zhai, S. Dong, Bifunctional fluorescent carbon nanodots: green synthesis via soy milk and application as metal-free electrocatalysts for oxygen reduction, Chem. Comm. 48 (75) (2012) 9367–9369, https://doi.org/10.1039/c2cc33844k.
[41] Yue Xu, Chun-Jing Tang, Hong Huang, Chao-Qun Sun, Y.K. Zhang, Qun-Feng Ye, Ai-Jun Wang, Green synthesis of fluorescent carbon quantum dots for detection of Hg^{2+}, Chin. J. Anal. Chem. 42 (9) (2014) 1252–1258, https://doi.org/10.1016/S1872-2040(14)60765-9.
[42] Y. Zhao, Y. Zhang, X. Liu, H. Kong, Y. Wang, G. Qin, P. Cao, X. Song, X. Yan, Q. Wang, H. Qu, Novel carbon quantum dots from egg yolk oil and their haemostatic effects, Sci. Rep. 7 (2017), 4452, https://doi.org/10.1038/s41598-017-04073-1.
[43] M. Zhou, Z. Zhou, A. Gong, Y. Zhang, Q. Li, Synthesis of highly photoluminescent carbon dots via citric acid and Tris for iron (III) ions sensors and bioimaging, Talanta 143 (2015) 107–113, https://doi.org/10.1016/j.talanta.2015.04.015.
[44] R. Atchudan, T.N.J.I. Edison, M. Shanmugam, S. Perumal, T. Somanathan, Y. R. Lee, Sustainable synthesis of carbon quantum dots from banana peel waste using hydrothermal process for in vivo bioimaging, Phys. E Low Dimens. Syst. Nanostruct. 126 (2021), 114417, https://doi.org/10.1016/j.physe.2020.114417.
[45] F.A. Wu, H. Su, K. Wang, W.K. Wong, X. Zhu, Facile synthesis of N-rich carbon quantum dots from porphyrins as efficient probes for bioimaging and biosensing in living cells, Int J. Nanomed. 12 (2017) 7375, https://doi.org/10.2147/IJN.S147165.
[46] A.G. El-Shamy, New free-standing and flexible PVA/Carbon quantum dots (CQDs) nanocomposite films with promising power factor and thermoelectric power applications, Mater. Sci. Semicond. 100 (2019) 245–254, https://doi.org/10.1016/j.mssp.2019.04.004.
[47] Z. Ramezani, M. Qorbanpour, N. Rahbar, Green synthesis of carbon quantum dots using quince fruit (Cydonia oblonga) powder as carbon precursor: application in cell imaging and As^{3+} determination, Colloids Surf. A Physicochem. Eng. Asp. 549 (2018) 58–66, https://doi.org/10.1016/j.colsurfa.2018.04.006.
[48] D. Kumar, K. Singh, V. Verma, H.S. Bhatti, Synthesis and characterization of carbon quantum dots from orange juice, J. Bionanosci. 8 (2014) 274–279, https://doi.org/10.1166/jbns.2014.1236.
[49] P. Wu, W. Li, Q. Wu, Y. Liu, S. Liu, Hydrothermal synthesis of nitrogen-doped carbon quantum dots from microcrystalline cellulose for the detection of Fe^{3+} ions in an acidic environment, RSC Adv. 7 (70) (2017) 44144–44153, https://doi.org/10.1039/C7RA08400E.
[50] H.J. Yashwanth, S.R. Rondiya, N.Y. Dzade, S.D. Dhole, D.M. Phase, K. Hareesh, Enhanced photocatalytic activity of N, P, co-doped carbon quantum dots: an insight from experimental and computational approach, Vacuum 180 (2020), 109589, https://doi.org/10.1016/j.vacuum.2020.109589.
[51] V. Ţucureanu, A. Matei, A.M. Avram, FTIR spectroscopy for carbon family study, Crit. Rev. Anal. Chem. 46 (6) (2016) 502–520, https://doi.org/10.1080/10408347.2016.1157013.
[52] T. Fan, W. Zeng, W. Tang, C. Yuan, S. Tong, K. Cai, Y. Liu, W. Huang, Y. Min, A. J. Epstein, Controllable size-selective method to prepare graphene quantum dots from graphene oxide, Nanoscale Res. Lett. 10 (2015), 55, https://doi.org/10.1186/s11671-015-0783-9.
[53] N. Architha, M. Ragupathi, C. Shobana, T. Selvankumar, P. Kumar, Y.S. Lee, R. K. Selvan, Microwave-assisted green synthesis of fluorescent carbon quantum dots from Mexican Mint extract for Fe^{3+} detection and bio-imaging applications, Environ. Res. 199 (2021), 111263, https://doi.org/10.1016/j.envres.2021.111263.
[54] M.S. Ardestani, Z. Zaheri, P. Mohammadzadeh, A. Bitarafan-Rajabi, S. M. Ghoreishi, Novel manganese carbon quantum dots as a nano-probe: Facile synthesis, characterization and their application in naproxen delivery (Mn/CQD/SiO_2@naproxen), Bioorg. Chem. 115 (2021), 105211, https://doi.org/10.1016/j.bioorg.2021.105211.
[55] G. El Fawal, H. Hong, X. Mo, H. Wang, Fabrication of scaffold based on gelatin and polycaprolactone (PCL) for wound dressing application, J. Drug. Deliv. Sci. Technol. 63 (2021), 102501, https://doi.org/10.1016/j.jddst.2021.102501.
[56] A. Mohebbi, M.A. Farajzadeh, A. Mahmoudzadeh, A. Etemady, Combination of poly (ε–caprolactone) grafted graphene quantum dots–based dispersive solid phase extraction followed by dispersive liquid–liquid microextraction for extraction of some pesticides from fruit juices prior to their quantification by gas chromatography, Microchem. J. 153 (2020), 104328, https://doi.org/10.1016/j.microc.2019.104328.
[57] H.M. Alhusaiki-Alghamdi, The spectroscopic and physical properties of PMMA/PCL blend incorporated with graphene oxide, Results Phys. 24 (2021), 104125, https://doi.org/10.1016/j.rinp.2021.104125.
[58] R.U. Rao, B. Venkatanarayana, K.N.S. Suman, Enhancement of mechanical properties of PLA/PCL (80/20) blend by reinforcing with MMT nanoclay, Mater. Today Proc. 18 (2017) 85–97, https://doi.org/10.1016/j.matpr.2019.06.280.

[59] R. Ekambaram, S. Saravanan, V.P.S. Babu, S. Dharmalingam, Fabrication and evaluation of Docetaxel doped ZnO nanoparticles incorporated PCL nanofibers for its hemocompatibility, cytotoxicity and apoptotic effects against A549, Materialia 21 (2022), 101278, https://doi.org/10.1016/j.mtla.2021.101278.
[60] R. Bayan, N. Karak, Bio-based hyperbranched polymer-supported oxygeneous graphitic-carbon nitride dot as heterogeneous metal-free solar light photocatalyst for oxidation and reduction reactions, Appl. Surf. Sci. 514 (2020), 145909, https://doi.org/10.1016/j.apsusc.2020.145909.
[61] N. Singh, U. Batra, K. Kumar, A. Mahapatro, Evaluation of corrosion resistance, mechanical integrity loss and biocompatibility of PCL/HA/TiO_2 hybrid coated biodegradable ZM21 Mg alloy, J. Magnes. Alloy. 10 (11) (2022) 3179–3204, https://doi.org/10.1016/j.jma.2021.10.004.
[62] J.J.P. Barros, I.D. Silva, S. dos, N.G. Jaques, M.V.L. Fook, R.M.R. Wellen, Influence of PCL on the epoxy workability, insights from thermal and spectroscopic analyses, Polym. Test. 89 (2020), 106679, https://doi.org/10.1016/j.polymertesting.2020.106679.
[63] T. Elzein, M. Nasser-Eddine, C. Delaite, S. Bistac, P. Dumas, FTIR study of polycaprolactone chain organization at interfaces, J. Colloid Interface Sci. 273 (2) (2004) 381–387, https://doi.org/10.1016/j.jcis.2004.02.001.
[64] X. Zhou, P. Ma, A. Wang, C. Yu, T. Qian, S. Wu, J. Shen, Dopamine fluorescent sensors based on polypyrrole/graphene quantum dots core/shell hybrids, Biosens. Bioelectron. 64 (2015) 404–410, https://doi.org/10.1016/j.bios.2014.09.038.
[65] G. Kandhol, H. Wadhwa, S. Chand, S. Mahendia, S. Kumar, Study of dielectric relaxation behavior of composites of poly (vinyl alchohol) (PVA) and reduced graphene oxide (RGO), Vacuum 160 (2019) 384–393, https://doi.org/10.1016/j.vacuum.2018.11.051.
[66] A.M. El-Sawy, M.H. Abdo, M.A. Darweesh, N.A. Salahuddin, Synthesis of modified PANI/CQDs nanocomposite by dimethylgyloxime for removal of Ni (II) from aqueous solution, Surf. Interfaces 26 (2021), 101392, https://doi.org/10.1016/j.surfin.2021.101392.
[67] X. Jian, H.-m Yang, J.-g Li, E.-h Zhang, L.-l Cao, Z.-h Liang, Flexible all-solid-state high-performance supercapacitor based on electrochemically synthesized carbon quantum dots/polypyrrole composite electrode, Electrochim. Acta 228 (2017) 483–493, https://doi.org/10.1016/j.electacta.2017.01.082.
[68] A. Irimia, G.E. Ioanid, T. Zaharescu, A. Coroabă, F. Doroftei, A. Safrany, C. Vasile, Comparative study on gamma irradiation and cold plasma pretreatment for a cellulosic substrate modification with phenolic compounds, Radiat. Phys. Chem. 130 (2017) 52–61, https://doi.org/10.1016/j.radphyschem.2016.07.028.
[69] H. Dhakal, A. Bourmaud, F. Berzin, F. Almansour, Z. Zhang, D.U. Shah, J. Beaugrand, Mechanical properties of leaf sheath date palm fibre waste biomass reinforced polycaprolactone (PCL) biocomposites, Ind. Crop. Prod. 126 (2018) 394–402, https://doi.org/10.1016/j.indcrop.2018.10.044.
[70] E. Cottam, D.W.L. Hukins, K. Lee, C. Hewitt, M.J. Jenkins, Effect of sterilisation by gamma irradiation on the ability of polycaprolactone (PCL) to act as a scaffold material, Med. Eng. Phys. 31 (2009) 221–226, https://doi.org/10.1016/j.medengphy.2008.07.005.
[71] J. Parameswaranpillai, M.R. Sanjay, S. Siengchin, S.K. Sidhardhan, S. Jose, N. V. Salim, N. Hameed, Intermolecular hydrogen bonding in developing nanostructured epoxy shape memory thermosets: effects on morphology, thermo-mechanical properties and surface wetting, Polym. Test. 81 (2020), 106279, https://doi.org/10.1016/j.polymertesting.2019.106279.
[72] M. Cobos, J.R. Ramos, D.J. Guzmán, M.D. Fernández, M.J. Fernández, PCL/POSS nanocomposites: effect of POSS derivative and preparation method on morphology and properties, Polymers 11 (2019) 33, https://doi.org/10.3390/polym11010033.
[73] S. Wilczewski, K. Skorczewska, J. Tomaszewska, K. Lewandowski, J. Szulc, T. Runka, Manufacturing homogenous PVC/graphene nanocomposites using a novel dispersion agent, Polym. Test. 91 (2020), 106868, https://doi.org/10.1016/j.polymertesting.2020.106868.
[74] C.L. Custodio, P.J.M. Broñola, S.R. Cayabyab, V.U. Lagura, J.R. Celorico, B. A. Basilia, Powder loading effects on the physicochemical and mechanical properties of 3D printed poly lactic acid/hydroxyapatite biocomposites, Int. J. Bioprint. 7 (1) (2021) 112–122, https://doi.org/10.18063/ijb.v7i1.326.
[75] J.A. Puértolas, M. Castro, J.A. Morris, R. Ríos, A. Ansón-Casaos, Tribological and mechanical properties of graphene nanoplatelet/PEEK composites, Carbon 141 (2019) 107–122, https://doi.org/10.1016/j.carbon.2018.09.036.
[76] S. Kim, J. Kim, M. Kim, M. Cho, Y. Lee, Aqua-processable carbon quantum dot–assisted resilient polymer binder for advanced lithium-sulfur batteries, Int. J. Energy Res. 45 (15) (2021) 21050–21057, https://doi.org/10.1002/er.7162.
[77] M.C. Azevedo, R.L. Reis, M.B. Claase, D.W. Grijpma, J. Feijen, Development and properties of polycaprolactone/hydroxyapatite composite biomaterials, J. Mater. Sci. Mater. Med. 14 (2) (2003) 103–107, https://doi.org/10.1023/A:1022051326282.
[78] E. Díaz, I. Sandonis, M.B. Valle, In vitro degradation of poly (caprolactone)/nHA composites, J. Nanomater. 185 (2014) 185, https://doi.org/10.1155/2014/802435.
[79] M. Bartnikowski, T.R. Dargaville, S. Ivanovski, D.W. Hutmacher, Degradation mechanisms of polycaprolactone in the context of chemistry, geometry and environment, Prog. Polym. Sci. 96 (2019) 1–20, https://doi.org/10.1016/j.progpolymsci.2019.05.004.
[80] H.R. Bakhsheshi-Rad, A.F. Ismail, M. Aziz, Z. Hadisi, M. Omidi, X. Chen, Antibacterial activity and corrosion resistance of Ta_2O_5 thin film and electrospun PCL/MgO-Ag nanofiber coatings on biodegradable Mg alloy implants, Ceram. Int. 45 (9) (2019) 11883–11892, https://doi.org/10.1016/j.ceramint.2019.03.071.
[81] Y.Q. Wang, J.Y. Cai, Enhanced cell affinity of poly (L-lactic acid) modified by base hydrolysis: Wettability and surface roughness at nanometer scale, Curr. Appl. Phys. 7 (2007) 108–111, https://doi.org/10.1016/j.cap.2006.11.027.